2022

SELF-OSCILLATING INDUCTION HEATER

Patrick Rice
Michigan Technological University, parice@mtu.edu

SELF-OSCILLATING INDUCTION HEATER

By

Patrick Rice

A REPORT

Submitted in partial fulfillment of the requirements for the degree of

MASTER OF SCIENCE

In Electrical and Computer Engineering

MICHIGAN TECHNOLOGICAL UNIVERSITY

2022

This report has been approved in partial fulfillment of the requirements for the Degree of MASTER OF SCIENCE in Electrical and Computer Engineering.

Department of Electrical and Computer Engineering

Report Advisor:	*Dr. Wayne W. Weaver*
Committee Member:	*Dr. Paul L. Bergstrom*
Committee Member:	*Prof. John T. Lukowski*
Department Chair:	*Dr. Jin W. Choi*

Contents

List of Figures

List of Tables

Abstract

This report develops a control system to keep an induction heater in resonance. When a metallic workpiece is inserted in the air core of the workcoil, the resonant frequency changes. Different workpiece materials affect the resonant frequency and power. This presents a problem since changing the resonant frequency of the circuit while keeping the frequency constant reduces the maximum power of the circuit. Finite element analysis is used to find the circuit parameters of the workcoil and workpiece interaction. A non-linear controller which oscillates based on the resonant frequency of an LC tank is created. Nyquist and describing function analysis is used to find sustained oscillation points of the circuit. A hardware induction heater with a non-linear controller is created to prove the design.

Chapter 1

Introduction

Induction heating is a method to heat ferrous and non-ferrous metals using time-varying magnetic fields. A workcoil is constructed from a highly conductive material, usually copper. The workpiece is made out of a conductive metal that couples the magnetic field. The field from the workcoil creates eddy currents within the workpiece due to Faraday's Law. Due to I^2R joule heating and hysteresis effects, the workpiece increases in temperature [1][2].

The advantages of induction heating are fast heating, efficiency, improved control of temperature, and cleaner operation. Induction heating is used in industrial, domestic, and medical applications. Industrial uses consist of melting, surface treatment, and annealing. Domestic applications include induction appliances. Medical uses are

sterilization of surgical instruments and specialized therapies [2].

One of the challenges of induction heating is the variability of circuit parameters due to permeability, material type, and temperature of the workpiece. This changes the resonant point of the coupled circuit. When the resonant point changes, it causes fluctuations in power, increased losses due to hard switching, and results in a low power factor for constant frequency converters. Tracking the resonant frequency of the circuit and operating the converter close to or at the resonant frequency ensures maximum power transfer to the workpiece.

This project report presents a self-oscillating circuit used to keep an induction heater in resonance. It uses two comparators that take current feedback from the RLC tank circuit to directly actuate a full-bridge inverter. Deadtime between switching is included in the design to ensure shoot-through does not occur.

Chapter 2

Background

2.1 Basic Topologies

In this chapter, converter topology and control methods are discussed for induction heaters. Converter topology determines many aspects of an induction heater. There are three main topologies, full-bridge, half-bridge, and single-switch [3]. The converters are shown in Figure 2.1. A full-bridge converter has four switches where two stacked switches form one leg of the converter. Both legs are placed together with the load in-between. This configuration supplies double the supply voltage across the load due to alternate sides of the load being grounded or at the supply voltage. The half-bridge converter consists of only one leg of a full-bridge converter. The other leg

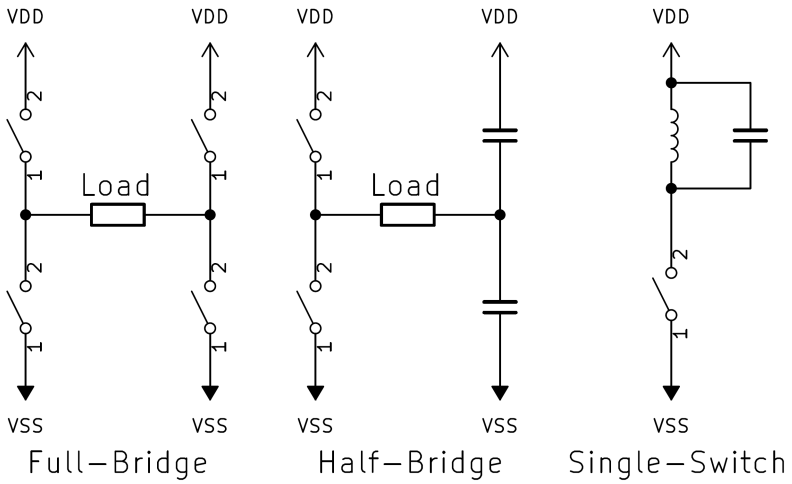

Figure 2.1: The most common topologies for induction heaters include full-bridge, half-bridge, and single-switch designs.

is replaced with two stacked capacitors. There is also a modification to this converter that neglects the capacitor stack and ties the load to the negative rail of the power supply. The single-switch converter has only one switch placed on the low side of the load. The input to these converters can be an AC-DC converter making it a two-stage converter. If AC is fed through a rectifier with minimal filtering, it is considered an AC-AC converter [3].

An example of a half-bridge induction heater is in the paper "A 50-150 kHz Half-Bridge Inverter for Induction Heating Applications" by Kamli, Yamamoto, and Abe [4]. The power supply is 200V 60Hz three-phase with a variac. The input voltage is rectified using a three-phase bridge rectifier. This is fed into the half-bridge without filtering capacitors making this an AC-AC converter from the previous definition. The switches are insulated gate bipolar transistors (IGBTs). The resonant circuit consists of a parallel LC circuit in series with a capacitor. Having a series capacitor

helps with no-load regulation and short-circuit conditions according to the authors. The workpiece is made out of steel and the workcoil is made out of seven turns of copper tubing. The stacked capacitors are in parallel with the resistors. This makes the voltage of the node at the mid-point of the supply. The switches are activated alternately. When the top switch is on, the current flows from the positive supply to the negative through the load charging up the bottom capacitor. When the bottom switch turns on current flows through the top capacitor, the load, and then the bottom switch.

Grajales and Lee present a full-bridge induction heater in [5]. The converter load consists of a transformer in series with a capacitor on the primary. A series RLC circuit is on the secondary. The switches are MOSFETs due to the high switching frequency of 500kHz. From Figure 2.1, the control system operates the switches in alternating pairs. The first pair is the top left and bottom right switch. The second pair is the top right and bottom right switch. When the first pair is turned on, current flows from to top left switch, through the load, and out the bottom right switch. The second pair operates on the same principle. Unlike the half-bridge, the node voltages are either at the positive or negative supply, not at the midpoint.

In the paper, "A 3.6kW Single-ended Resonant Inverter for Induction Heating Applications", a simple single-switch converter is presented [6]. This converter is also called a class E converter. Zero voltage switching (ZVS) is essential in this converter

to reach high efficiency. When the switch turns on, the current ramps up through the inductor. A series LR circuit is the equivalent circuit at this stage. When the switch is turned off, quasi-resonance begins between the L and C components. The equivalent circuit now represents a series RLC circuit between the capacitor, inductor, and the series resistance of the inductor. The inductor current falls and the voltage across the switch rises. When the inductor current goes below zero the voltage across the switch starts falling. The voltage across the open switch rises to approximately 1200-1500V at full power requiring a high-voltage switch. When the voltage across the switch reaches zero and heads negative, the reverse diode in the IGBT clamps the voltage at zero volts. At this point, the gate pulse is reapplied to repeat the cycle.

2.2 Control Systems

From [2], there are mainly two aspects to control in an induction heating system. The first is the power of the system. Due to the variable nature of the load, the output power varies. Constant power is ideal due to thermal or power targets imposed by the user. The power is sometimes manually controlled for example in [4] using a variac, but this is not ideal since the power can increase substantially if the load is removed from the induction heater. For the second aspect, the frequency has to be controlled because the system consists of inductive and capacitive elements which usually have a resonant or anti-resonant frequency attached to them. The frequency

is usually tuned around the resonant/anti-resonant frequency for maximum power transfer. The two aspects can also be combined into one control strategy where the power is controlled by shifting the frequency away from the resonant frequency. The single-switch topology does not control the frequency of resonance since it relies on the natural ringing of the LC circuit.

Pulse width modulation (PWM) is a constant frequency control method where the output power is controlled by varying the pulse width. This control technique is easily achieved. The cost is the reduced efficiency due to hard-switching [3]. To achieve soft-switching, the PWM technique is combined with zero voltage switching (ZVS). This is done with phase shifting of the PWM signal. In [5], the authors use the ZVS-PWM method. When the converter is operated at full power, the frequency is operated slightly above the resonant frequency to ensure ZVS condition. This allows the MOSFET to switch during the reverse diode conduction period. If the duty cycle were to decrease with a lower power request, keeping the frequency constant would result in the ZVS being lost. To compensate for this, the controller increases the switching frequency to ensure that the MOSFETs are switching during the reverse diode conduction period.

Two separate control systems and power electronic circuits are also a possibility for a resonant inverter. In [7], the authors describe a three-phase controlled rectifier being used to vary the DC bus voltage. This automatically would control the power of

the circuit with a feedback circuit. The second part is an H-bridge switching at the resonant frequency for the frequency control. This technique uses more components than a converter with only one stage. This problem is solved with a pulse density modulation (PDM) technique described in the paper. Subtracting the power reference from the actual power, an error signal is created. This error signal is fed through a PID controller. The output of the controller is a comparator. If the PID value is above zero meaning that the actual power is lower than the reference power, the comparator outputs a one. If the PID value is lower than zero meaning that the actual power is above the reference, the comparator outputs a zero. The output of the comparator is fed through a flip-flop with clock input. The clock pulses every time the current in the RLC circuit crosses zero. A clock pulse sends the value of the input to the output and latches it. If the output of the comparator is zero, the voltage pulse across the LC circuit is skipped for the cycle. If the comparator is one, a voltage pulse is sent across the LC circuit. Skipping a pulse across the LC circuit causes the average power to decrease. Pulsing the LC circuit increases the average power. This regulates the circuit at constant power due to the feedback mechanism called PDM.

Tracking the resonant frequency is essential to the operation of an induction heater. The most common technique is using a phase-locked loop (PLL). In [4], a PLL tracks the resonant frequency by measuring the voltage across the series capacitor. The voltage across the series capacitor leads the control signal to the switches by 90°

during resonance. This relies on a phase shifter, two comparators, an integrator, a low pass filter, and an MC14046B PLL IC to accomplish resonant tracking. An alternate approach that requires less complex circuitry to resonant tracking is presented in "Self-Oscillating Electronic Ballast Design Based on the Point of View of Control System" [8]. The application for this paper is an electronic ballast for fluorescent tubes. It uses non-linear relay control based on the polarity of the current signal through a series/parallel RLC circuit. This control system is expanded on in this report in the application of induction heating.

Chapter 3

Theory

3.1 Series and Parallel LC Circuits

Two of the simplest LC circuits are the series and parallel configuration shown in Figure 3.1.

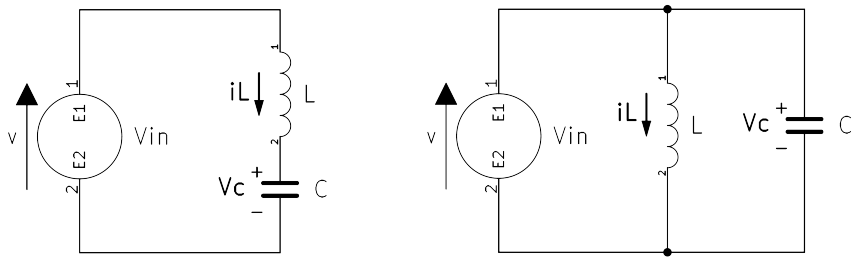

Figure 3.1: The series LC circuit on the left consists of an inductive and capacitive element in series. On the right, a parallel LC circuit consists of an inductive and capacitive element in parallel. A voltage source is across both the series and parallel circuits.

When the reactance of the inductor and capacitor in a series or parallel circuit equal each other,

$$X_L = X_C \tag{3.1}$$

$$sL = \frac{1}{sC} \tag{3.2}$$

a zero (zero reactance) or pole (infinite reactance) is formed respectively. Replacing s with $j\omega$ and solving for frequency results in

$$\omega = \pm\frac{j}{\sqrt{LC}}. \tag{3.3}$$

If the real part is taken from equation (3.3)

$$\omega = \frac{1}{\sqrt{LC}}. \tag{3.4}$$

The impedance of a series LC circuit adds both the capacitive and inductive elements together

$$z_{series} = \frac{1}{sC} + sL. \tag{3.5}$$

When s is substituted for $j\omega$

$$z_{series} = j\omega L - \frac{j}{\omega C}. \tag{3.6}$$

Applying equation (3.4) to (3.6) results in zero impedance. This shows for a series LC circuit at resonance, the impedance drops to zero. When the frequency is zero or infinite, the impedance is complex infinite.

A similar result occurs with a parallel circuit. The total impedance is found with

$$z_{parallel} = \frac{sL}{s^2LC + 1}. \tag{3.7}$$

Replacing s with $j\omega$ results in

$$z_{parallel} = \frac{j\omega L}{\omega^2 LC + 1}. \tag{3.8}$$

Substituting equation (3.4) into (3.8) results in complex infinite impedance. When the frequency is zero or infinite, the impedance is zero.

3.2 Driven Series RLC Circuit

For series RLC systems driven with a voltage source, the driven resonant frequency differs from the natural resonant frequency calculated in (3.4). In [9], the natural frequency is multiplied by $\sqrt{1-\zeta^2}$ to find the point of resonance

$$\omega_r = \omega_n \sqrt{1-\zeta^2}. \tag{3.9}$$

Where ζ is the damping ratio calculated with

$$\zeta = \frac{1}{2Q}. \tag{3.10}$$

The quality factor is the ratio of stored energy to dissipated energy in one cycle. The quality factor Q of the RLC circuit is calculated with

$$Q = \frac{\sqrt{LC}}{R}. \tag{3.11}$$

This resonant frequency shifting phenomenon can also be observed by looking at the eigenvalues of the RLC circuit in

$$-\frac{R}{2L} \pm \sqrt{\left(\frac{R}{2L}\right)^2 - \left(\frac{1}{LC}\right)}. \tag{3.12}$$

The resistance of the circuit modifies both the damping coefficient $-R/2L$ and the complex part. For an underdamped system, $(R/2L)^2$ has to be lower than $1/LC$ [10]. For a resonant peak to occur, the system has to be underdamped. For quality factors over five, the driven resonant frequency can be approximated with the natural frequency.

3.3 Transformer and Series Equivalent Circuit Model

The induction workcoil to workpiece interaction can be described as a transformer with a shorted secondary turn as the workpiece [11]. Following [7], a model of the induction work-coil and workpiece is created. When the workcoil is unloaded, only the Lp inductance and Rp resistance are present. When a workpiece is inserted in the center of the inductor, Ls and Rs of the workpiece present an additional load shown in Figure 3.2(a).

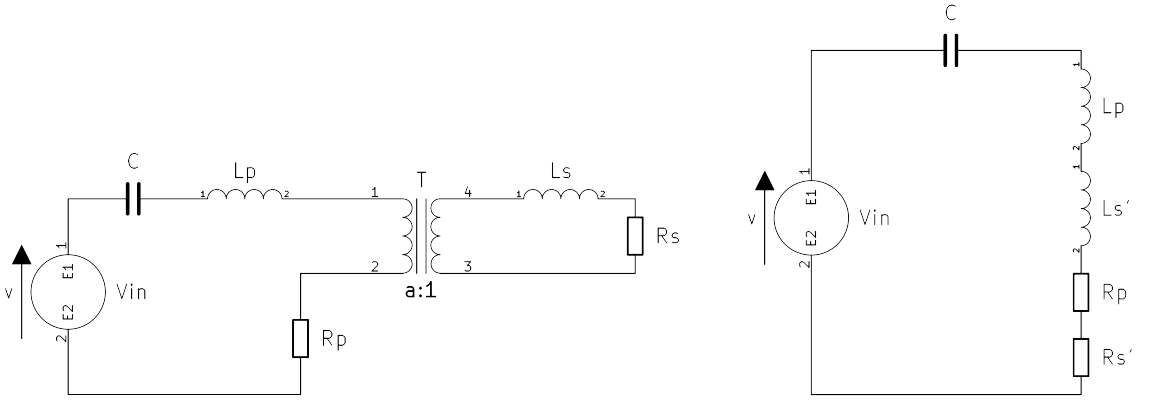

(a) The workcoil/workpiece interaction can be described as a transformer linking the workcoil with a series LC secondary as the workpiece

(b) The simplified circuit reflects the secondary to the primary as a resistance Rs' and inductance Ls'

Figure 3.2: A series RLC circuit represents a workcoil with a series capacitor. A transformer with a series LC circuit is added to model the workcoil/-workpiece coupling. This model is simplified using transformer impedance reflection.

Ls and Rs are reflected across the transformer with

$$Ls' = Ls \cdot a^2 \tag{3.13}$$

$$Rs' = Rs \cdot a^2 \tag{3.14}$$

and added in series with the Lp and Rp components shown in Figure 3.2(b). a is the number of turns of the workcoil. This creates the series equivalent circuit (SEC) model of an induction heater [11].

3.4 Series RLC Tank Circuit with Transformer

An impedance transformer is needed to couple a high-voltage H-bridge circuit to a low-impedance RLC tank circuit. A tee transformer model from [12] is used as a starting point in Figure 3.3(a).

The load resistance from the paper is replaced with a series capacitance to form the series RLC circuit. The primary and reflected components from the SEC model are lumped into Ls and Rs in this extended model. The input voltage, primary components, and mutual components are reflected to the secondary side. To simplify the model further, Rp', Lp', and Rc' are assumed to be small compared with the other component values. This leads to the creation of the simplified model, Figure 3.3(b).

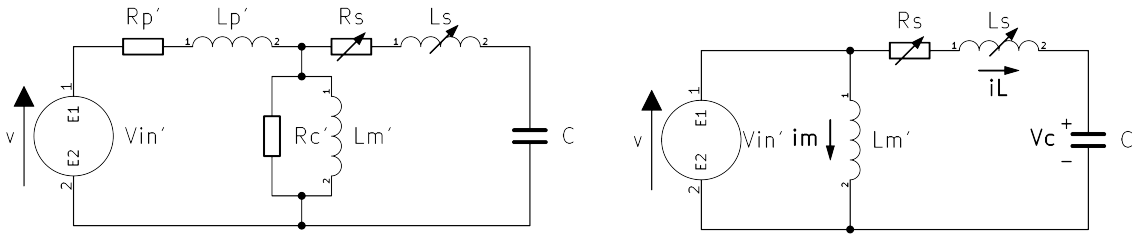

(a) A non-ideal transformer is modeled using the tee model. The primary resistance, inductance, voltage, core loss, and mutual inductance are reflected to the secondary. The secondary LR components represent the combined inductance and resistance of the workcoil/workpiece.

(b) The model is simplified by removing the primary resistance, inductance, and core loss.

Figure 3.3: The tee model of the transformer represents the toroidal transformer which injects energy into the RLC tank circuit.

This model only includes the mutual inductance formed by the transformer winding and the series RLC circuit in parallel. The primary to secondary reflected values are calculated using

$$Vin' = Vin/b \tag{3.15}$$

$$Lm' = Lm/b^2 \tag{3.16}$$

where b is the turn ratio of the transformer. The circuit model forms a series/parallel circuit with a resonant and anti-resonant frequency.

3.4.1 State Equation Derivation

From Figure 3.3(b), the states are identified from the circuit as the current through the workcoil iL, the mutual inductance lm, and the voltage across the capacitor Vc. The change in inductor currents $\dot{im}$

$$0 = Vin - Lm\frac{dim}{dt} \tag{3.17}$$

$$\dot{im} = \frac{Vin}{Lm} \tag{3.18}$$

and $\dot{iL}$

$$0 = Vin - iL \cdot Rs - Ls\frac{diL}{dt} - Vc \tag{3.19}$$

$$\dot{iL} = \frac{1}{Ls}(Vin - iL \cdot Rs - Vc) \tag{3.20}$$

were found by taking Kirchhoff's voltage law and applying it to the loops of the circuit in Figure 3.3(b) The voltage across the capacitor $\dot{V}c$

$$Vc = \frac{1}{C}\int iL\ dt \tag{3.21}$$

$$\dot{V}c = \frac{1}{C}iL \tag{3.22}$$

was found by differentiating equation (3.21). Replacing Vin with u, im with x_1, iL with x_2, and Vc with x_3 in equations (3.18),(3.20),(3.22) results in the final state equations for the RLC circuit

$$\dot{x}_1 = \frac{u}{Lm} \tag{3.23}$$

$$\dot{x}_2 = \frac{1}{Ls}(u - x_2 \cdot Rs - x_3) \tag{3.24}$$

$$\dot{x}_3 = \frac{1}{C}x_2. \tag{3.25}$$

3.5 Describing Function of Relay Non-linearity

The proposed control system relies on the secondary inductor current feedback, iL. The current flowing through the mutual inductance does not influence the current flowing through the RLC circuit because it is independent of the other states in the system.

A sign function is used to create the non-linear relay function

$$NL_{Relay} = Sign[x_2]. \tag{3.26}$$

Where the output of the sign function is negative or positive depending on the polarity of the input current, x_2. This determines the polarity of the voltage source across the transformer and the series RLC circuit.

The system has to meet four criteria in [13] before the describing function method can be used. The first assumption is that there is only a single non-linear component. The relay non-linearity is the only non-linear component in the system. The second assumption states the non-linearity must be time-invariant. There is no time function in the relay control system. The last assumption is that the non-linearity is odd. The nonlinearity is symmetric about the origin.

The system must have low-pass characteristics so only the fundamental of a sinusoid function running through the system is considered. In [8], the authors state that an RLC resonant system operating above the resonant frequency exhibits low-pass characteristics. The paper does not elaborate on what happens below and at the resonant frequency. The RLC transfer function from the applied voltage across the series RLC circuit to the current flowing through it

$$G_{RLC} = \frac{s}{L(s^2 + \frac{sR}{L} + \frac{1}{CL})} \tag{3.27}$$

has low pass characteristics above the resonant frequency. Below the resonant frequency, the system exhibits high pass characteristics. If a step function is applied

to this transfer function, the dominant frequency at the output will be the resonant frequency of the system. Due to the infinite frequency content of the step function, the system has low-pass characteristics due to the output frequency being the resonant frequency. This assumes that the frequency content of the step function is much larger than the resonant frequency if the rise time is finite.

To use Nyquist analysis, all functions have to be linear. A describing function is created to approximate the non-linear relay. An in-depth analysis is available in the Applied Nonlinear Control textbook written by Slotine and Li [13]. If a sinusoidal signal is fed into a non-linear block, the output $w(t)$ is usually periodic and non-linear. The output is expanded using Fourier series

$$w(t) = \frac{a_0}{2} + \sum_{n=1}^{\infty}[a_n cos(n\omega t) + b_n sin(n\omega t)]. \tag{3.28}$$

Due to the odd non-linearity assumption, the a_0 coefficient is zero. Due to the system having low pass characteristics, only the fundamental component of the Fourier series is needed. For a relay system, there is no phase shift from the input signal. This is due to the immediate switching as the input goes above and below zero. The a_1 coefficient is zero due to this. The describing function is found by solving for the b_1 coefficient divided by the input amplitude

$$N(A) = \frac{b_1}{A} = \frac{4}{\pi A}\int_0^{\pi/2} M sin(\omega t)\, d(\omega t) = \frac{4M}{\pi A} \tag{3.29}$$

where A is the input amplitude, M is the output amplitude. A plot of the normalized gain (N(A)/M) of the describing function in equation (3.29) is shown in Figure 3.4.

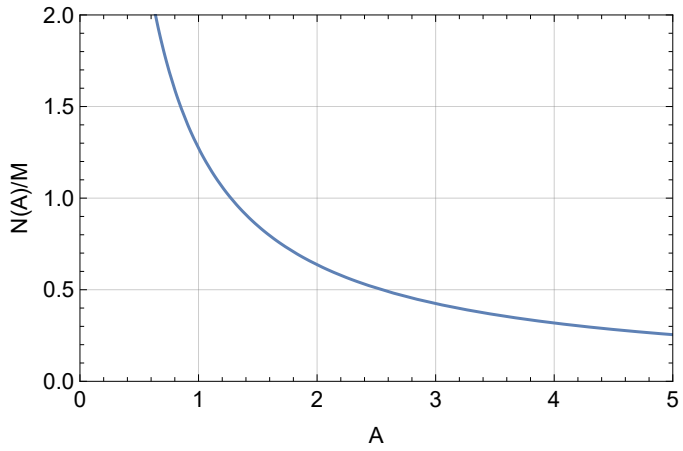

Figure 3.4: Normalized gain of the describing function of a relay non-linearity.

3.6 Nyquist Analysis

A relay non-linearity control system with positive feedback is used to actuate the voltage input based on the current through the system. Figure 3.5 describes a closed-loop linear system with positive feedback. G(s) represents the linear transfer function for the RLC circuit from voltage to current. The transfer function of the RLC circuit is shown in equation (3.27). H(s) represents a describing function for a non-linear

element.

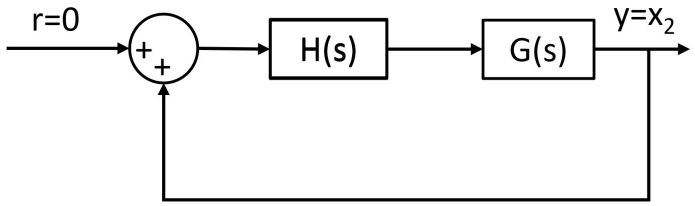

Figure 3.5: A positive feedback control system with a describing function for a relay as H(s) and a linear transfer function from voltage to current, G(s). Current from output y is fed back into the describing function.

The open loop transfer function of the linear system model is

$$G(s)H(s) = 1. \tag{3.30}$$

Replacing H(s) with the describing function, an equation for determining the existence of limit cycles is created

$$G(j\omega) = \frac{1}{N(A)}. \tag{3.31}$$

A Nyquist plot is formed when the left-hand side is plotted on a real/imaginary plane by varying ω from $-\infty$ to $+\infty$. The amplitude of the system is found when the right-hand side of the equation is plotted by varying A. When the curves intersect a solution to equation (3.31) is found. This solution predicts a limit cycle exists in the non-linear system.

Both 1/N(A) and G(jω) were plotted on a real imaginary plot in Figure 3.6 using

1.05μH for L, 10.6$\mu\Omega$ for R, and 1000μF for C. G(jω) encircles one in a clockwise direction. This creates an unstable zone where 1/N(A) traverses. 1/N(A) increases in amplitude. When the 1/N(A) line exits the unstable zone by crossing the G(jω) curve, it enters a stable zone. This causes it to stop at the resonant point. If 1/N(A) were to start outside of the circle, the system would settle until it reaches the intersection point. Solving for the second intersection point, the amplitude A is estimated to be 120.12(Apk) at a frequency of 30860.7 rad/s or 4.91kHz.

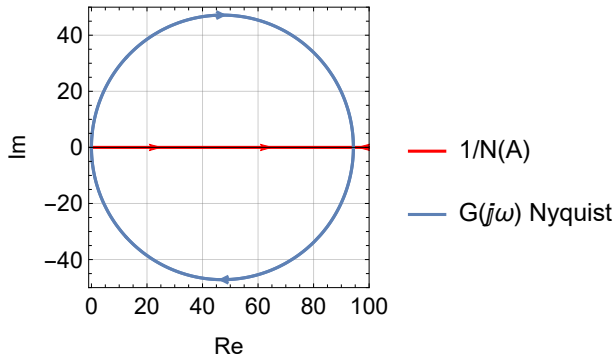

Figure 3.6: The Nyquist plot shows the result of plotting $G(j\omega)$ from -∞ to ∞ and 1/N(A) from A=0 to 3000. The intersection between the lines is the location of potential limit cycles.

From Figure 3.6, it was found that the point of resonance occurred at the second crossing of the imaginary axis. The first crossing occurs at ω=0. The critical point is one due to equation (3.30). G(s)H(s) cannot have clockwise encirclements or equal one to be stable.

With the series RLC circuit, for frequencies under resonance, the Nyquist plot of G(jω) is positive meaning that the circuit exhibits capacitive behavior (+Im). For

frequencies over the resonance frequency, the circuit is inductive (-Im). When the imaginary part equals zero of G(jω), the circuit shows resistive behavior. Since the Nyquist plot is showing current, the phase reference is the current. This means the phase polarity is the opposite of convention when voltage is used as the reference.

The closed loop system with the relay non-linearity was simulated with initial conditions of $x_1 = 0, x_2 = 0$ and $x_1 = 200, x_2 = 0$. The result of this simulation in the phase plane is shown in Figure 3.7. Starting at (0,0) resulted in the current becoming unstable with the amplitude growing. When the amplitude reaches a point estimated by the Nyquist analysis, the trajectory reaches a limit cycle. Starting at (200,0), the current reduces in amplitude until it again reaches the limit cycle. This verifies that there is a stable limit cycle in a $\pm$6V, $\pm$200A region around (0,0).

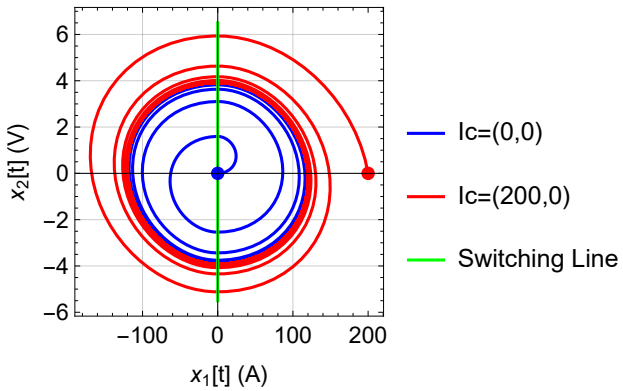

Figure 3.7: A simulation of an example series RLC circuit with a non-linear relay controller in phase plane is shown. The current through the RLC circuit is on the x-axis. The voltage across the capacitor is on the y-axis. The green shows the switching line of the controller. The red and blue lines show the initial conditions of current and voltage outside and inside the limit cycle respectively.

3.7 Skin Effect

The eddy current induced in the workpiece from the time-varying magnetic field from the workcoil is concentrated on the outside due to the skin effect. The skin depth equation is

$$\delta = \frac{1}{\sqrt{\pi f \mu_0 \mu_r \sigma}} \tag{3.32}$$

where δ is the skin depth, f is frequency, μ_0 is the vacuum permeability, μ_r is the relative permeability, and σ is the conductance of the workpiece material [14].

3.8 Power of Workcoil and Workpiece

The power dissipated by the combined workcoil and workpiece is defined as the current squared multiplied by the resistance in

$$P_{WC} = I^2 \, Rt. \tag{3.33}$$

To find the power dissipated in the workpiece the reflected resistance of the workpiece is found

$$Rs' = Rt - Rp \tag{3.34}$$

with the open load workcoil resistance Rp being subtracted from the combined resistance Rt [7]. The reflected resistance Rs' is substituted in for Rt in equation (3.33).

3.9 Hamiltonian

The Hamiltonian

$$H = \frac{1}{2}C\ V^2 + \frac{1}{2}L\ I^2 \tag{3.35}$$

of the series RLC circuit is found by summing the stored energy in each component. The energy stored in a capacitor is the first term $\frac{1}{2}C\ V^2$ [14]. The energy stored in an inductor is the second term $\frac{1}{2}L\ I^2$ [14].

Chapter 4

Circuit Parameters

4.1 Parameters and Construction

4.1.1 Workcoil and Workpiece

The workcoil is constructed with 0.25 inch (6.35mm) outside diameter (OD), and 0.19 inch (4.83mm) inside diameter (ID) copper refrigeration tubing. The tubing is coiled 10 times to form a 100mm ID and 100mm length cylinder shown in Figure 4.1. This makes a equal to 10 in equations (3.13) and (3.14). A fiberglass sleeve is over the workcoil to prevent short circuits and protect from high workpiece temperatures.

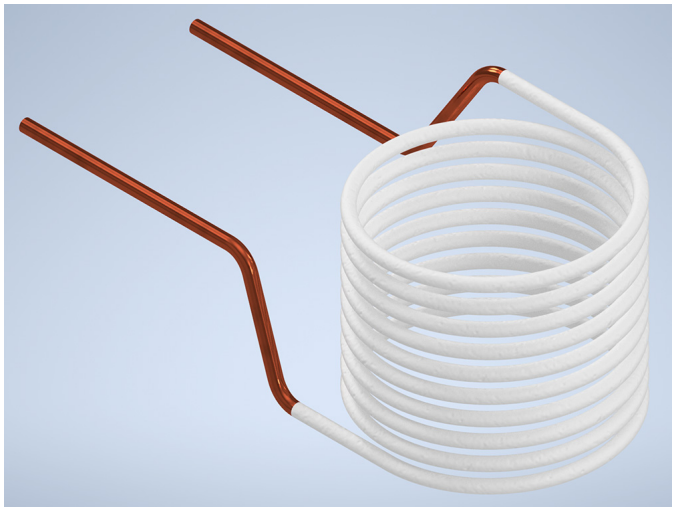

Figure 4.1: A rendering of the workcoil constructed in the project. 1/4" copper tubing is used. The coil is protected using fiberglass insulation in white.

The workpieces consist of 50mm OD by 100mm length solid cylinders made out of 6061 aluminum, 304 stainless steel, and 1006 steel. The workcoil model consists of a series resistance Rs and inductance Ls in Figure 3.3(b). This represents the combined resistance and inductance of the workcoil and reflected workpiece parameters.

The inductance and resistance parameters are found using the finite element analysis (FEA). Finite Element Method Magnetics (FEMM) version 4.2 software is used for this analysis. FEMM is a free 2D planar and axisymmetric solver for magnetic, electrostatic, and heat flow problems. The axisymmetric solver is used for this report. An axisymmetric model takes a three-dimensional model that is symmetric around one axis and uses a two-dimensional cross-section for analysis. The cross-sectional model is split up into many triangular regions shown in Figure 4.2. A high amount of elements in the skin effect region is used to model the eddy current effect accurately.

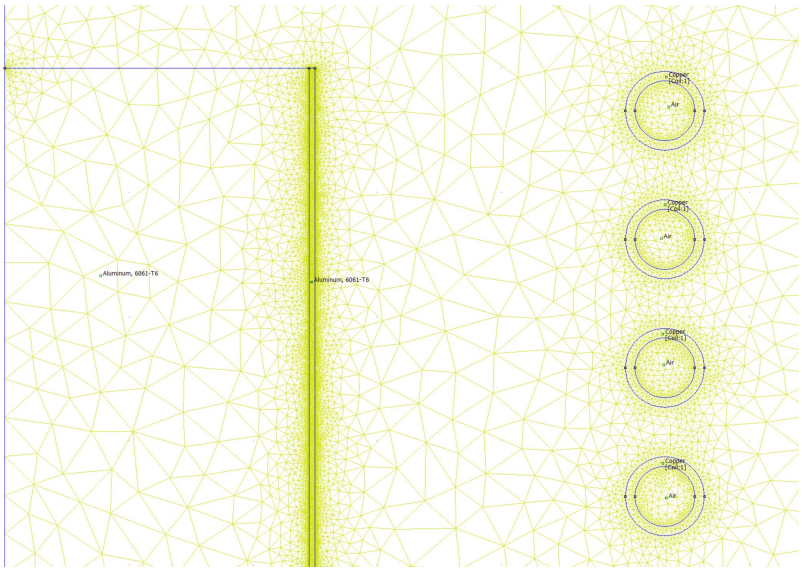

Figure 4.2: The workcoil has rotational symmetry. Axisymmetric FEA is used to approximate the 3D inductor and workpiece using a 2D plane. A triangular mesh in yellow is used for solving the magnetics problem. A small mesh is used for modeling the eddy currents of the workpiece. The materials of the workpiece, workcoil, and air gaps are specified.

To model eddy currents in the workpiece, a time-harmonic magnetic problem is created. The equation FEMM uses to solve time-harmonic magnetic problems is

$$\nabla \times \left(\frac{1}{\mu_{eff}(B)} \nabla \times a \right) = -j\omega\sigma a + \hat{J}_{src} - \sigma \nabla V \tag{4.1}$$

where μ_{eff} is the effective permeability, B is the magnetic field, a is the flux density in terms of the vector potential, σ is the conductivity, ω is the frequency, $\hat{J}_{src}$ is the phasor transform of the current sources, ∇V is an additional voltage gradient [15].

The workcoil is simulated using an empty coil and with the three workpiece materials.

The material properties are shown in Table 4.1. A relative permeability of one is used for air, 6061 aluminum, and 304 stainless steel. For 1006 Steel, a relative permeability of 1404 and a non-linear B-H curve is used shown in Figure 4.3. For the Nyquist analysis and simulation, a linear B-H curve is used. The test current used in the calculation is 100 amps peak. The frequency of the current is 20kHz. The flux density is shown in Figure 4.4. With no workpiece, the flux is distributed uniformly between the copper coils, Figure 4.4(a). The center of the workpieces does not have significant flux due to the skin effect. The aluminum workpiece in Figure 4.4(b) has less penetration of flux compared to the stainless steel workpiece in Figure 4.4(c). This is due to the higher conductivity of aluminum compared to stainless steel. The steel workpiece in Figure 4.4(d) has a high amount of flux density in the skin effect region due to a large relative permeability. This lowers the skin depth leading to a high flux density.

Material	μ_r	Conductivity (MS/m)	B-H Curve	δ (mm)
Air	1	0	Linear	∞
6061 Aluminum	1	24.59	Linear	0.72
304 Stainless Steel	1	1.45	Linear	2.96
1006 Steel	1404	5.8	Non-Linear	0.04

Table 4.1
Workpiece Material Properties

The inductance (flux/current) and resistance (voltage/current) of the workcoil were measured from the FEA analysis shown in Table 4.2. The real number for resistance represents the addition between the primary and reflected secondary resistances. The

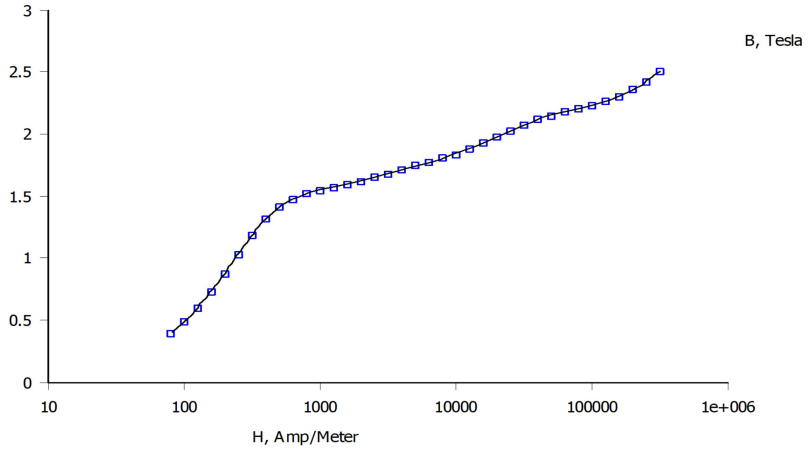

Figure 4.3: 1006 steel workpiece non-linear B-H curve used in FEA.

real number for inductance is the subtraction between the primary and reflected secondary inductance [10]. Only the real numbers are used in further analysis due to the focus on the primary values of resistance and inductance instead of the secondary values.

Workpiece Material	Flux/Current (μH)	Voltage/Current (mΩ)
No Workpiece	$6.77 - j4.67 \cdot 10^{-3}$	$10.3 + j850$
6061 Aluminum	$5.67 - j4.01 \cdot 10^{-2}$	$15.1 + j712$
304 Stainless Steel	$5.79 - j0.148$	$28.6 + j728$
1006 Steel	$6.96 - j1.23$	$164 + j875$

Table 4.2
Workcoil Parameters from FEA

The constructed workcoil was measured with a Hioki 3532-50 LCR meter at 20kHz. Open-short compensation was performed at 20kHz. The inductance measured 7.168μH, a 5.71% difference. The resistance measured 12.05mΩ, a 15.7% difference. Due to the variable contact resistance of the kelvin clamps between the short compensation and the measurement, the measured resistance is larger than the FEA

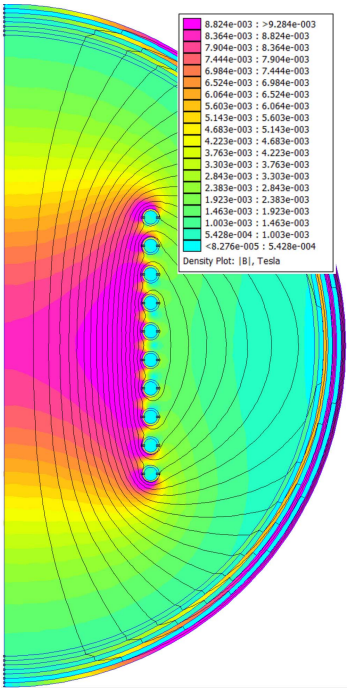

(a) No workpiece. Flux is distributed uniformly across the workcoil.

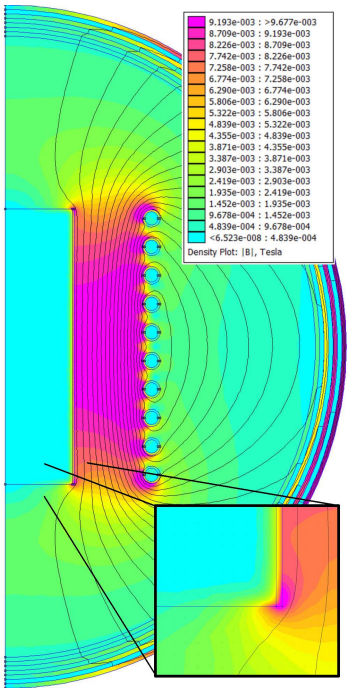

(b) 6061 Aluminum. Flux is concentrated between the workcoil and workpiece.

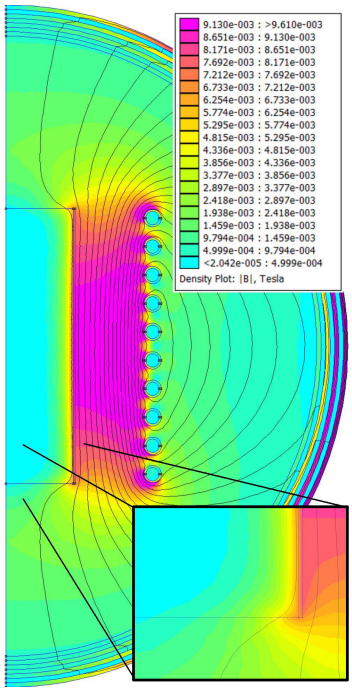

(c) 304 Stainless Steel. Flux penetrates deeper into the workpiece than aluminum due to lower conductivity.

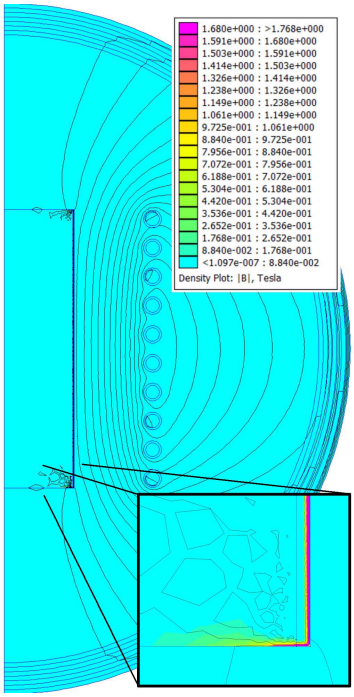

(d) 1006 Steel. A high relative permeability causes the skin depth to be very thin concentrating the flux.

Figure 4.4: FE analysis of workcoil/workpiece coupling flux density plots show relative skin depth consistent with calculated values.

result.

4.1.2 Capacitor Bank

The capacitance needed to match the inductance of the workcoil was chosen based on available values, cost, current, voltage, and the frequency of operation. A frequency near 20kHz was picked to prevent the induction heater from operating in the audible range. The value has to be near 9μF when solving equation (3.4) to resonate at 20kHz. The current and voltage requirements were found by simulating the circuit. A DC voltage of 250V and an approximate RMS current of 350A were chosen. These requirements necessitated the use of multiple capacitors in parallel due to the lack of off-the-shelve single capacitors with 9μF, 250V, and 350A capability. The Kemet R76 series was chosen due to the high RMS current capability compared to other capacitor series. The series features double-metalized polyester film for resonant applications with high voltage, current, and frequency. The specific capacitor picked for the capacitor bank was the R76MI33905050J because it had the highest current density per area out of the capacitors evaluated. It is a 0.39μF capacitor with 11 Arms current capability with a 250V maximum DC voltage. 32 capacitors are needed in parallel to meet both the current and capacitance limits. 36 capacitors were chosen to exceed the current specification. The final capacitance value is calculated to be 14.04μF. The resonant frequency was calculated with an open workcoil to be 16.32kHz.

The dielectric is polypropylene film for lower dielectric losses (tanδ) than a polyester film dielectric. The equivalent series resistance (ESR) was calculated with

$$ESR = \frac{tan\delta}{2\pi f_{test} C_{total}}. \tag{4.2}$$

Where $tan\delta$ is the dissipation factor, f_{test} is the test frequency, C_{total} is the total capacitance of the bank. Using values from the capacitor datasheet [16], the ESR is calculated to be 0.6801mΩ. The capacitance was measured with a Hioki 3532-50 LCR meter at 20kHz to be 14.28μF, a difference of 1.68%. The ESR was not measured because it is lower than the minimum impedance of 10mΩ from the meter datasheet. An LCR meter with a lower resistance measurement (0.1mΩ) capability should be used for this measurement.

A double-layer circuit board was fabricated using two-ounce copper. 41 capacitors can be populated on the circuit board in parallel. There are two 6.6mm holes for the copper tubing to fit through which is soldered for a low-resistance connection. Each side of the circuit board is filled with copper acting as the connection point for the capacitors. The assembled capacitor bank is shown in Figure 4.5.

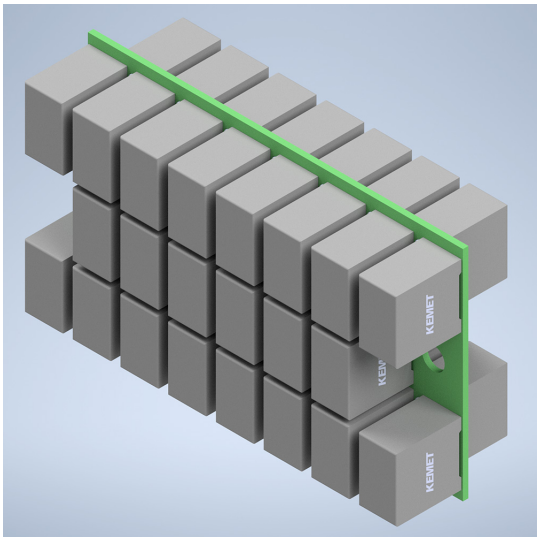

Figure 4.5: A 3D rendering of the capacitor bank. 36 0.39μF 250V capacitors in parallel were used. A low ESR leads to a 350Arms current capability.

4.1.3 Transformer

The transformer is a toroid shape. The primary winding is constructed from Litz wire. The secondary winding consists of the copper tubing used in the LC tank circuit. A primary voltage of 169.7V was selected since it is equal to the full-bridge rectified 120Vrms mains voltage. The calculated input current was 5.98A. The output power is 1000W. A power formula is used to determine the secondary voltage needed

$$V_{sec} = \sqrt{P_{out} R_{total}}. \tag{4.3}$$

The secondary voltage was calculated to be 3.97V with an aluminum workpiece. From

$$n1 = \frac{V_{prim}}{V_{sec}} n2 \tag{4.4}$$

the turns of the transformer are found. The secondary winding $n2$ consists of only one turn from the copper pipe. The number of windings needed is 43 turns. Based on the current, frequency, and availability, 100/35 Litz wire was used on the primary. The Litz wire has 100 strands of 35 AWG wire. The resistance was measured at 16.5 ohms/1000m at 20kHz which is equivalent to 17 AWG wire. Calculating the current density in circular mils/amp results in 531.9cmil/amp.

The core size was selected with the window area core area product

$$WaAc = \frac{P_{out} D_{cma}}{ktB_{max}f}. \tag{4.5}$$

Where D_{cma} is the current density in circular mils/amp, B_{max} is the maximum flux density in gauss of the transformer material, kt is the topology constant, f is the frequency of operation. Using 531.9 circular mils/amp, 1600 gauss, 0.0014 for the topology constant, and 20kHz for frequency, the WaAc needed is 11.87cm^4. The Ferroxcube TX55/32/18-3E6 toroidal ferrite core was chosen since it has a WaAc of 15.34cm^4. This exceeds the specification by 25.5%. The maximum flux density of the 3E6 material from Ferroxcube is 3900 gauss or 390mT at 25°C or 220mT at 100°C.

This exceeds the specification by 31.6% worst case. The completed transformer is shown in Figure 4.6.

Figure 4.6: A toroidal transformer injects energy into the RLC tank circuit. The secondary goes through the center consisting of 1/4" copper tubing.

The mutual inductance lm was calculated with

$$lm = al \cdot n1^2. \tag{4.6}$$

Where al is the inductance per square turn in nH/turn^2. Using 18400nH/turn^2 and 43 turns resulted in an inductance of 34.02mH. Reflecting the inductance from the primary to secondary results in a parallel inductance of 18.40μH. Using a Hioki 3532-50 LCR meter, the open-circuit parallel inductance of the physical transformer was measured to be 31.49mH at 20kHz. A difference of 7.72% from the calculated value. The parallel resistance was measured at 162.13kΩ. The parallel resistance of the transformer was not used in further simulations due to the high value. Shorting the secondary of the transformer with a section of 1/4" copper tubing resulted in a series inductance of 155.95μH and resistance of 1.873Ω, shown in Figure 4.7. The series

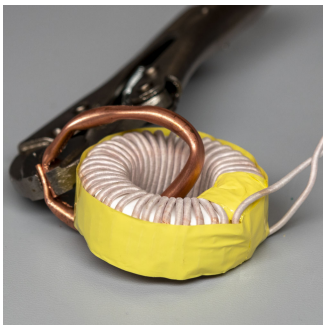

Figure 4.7: The secondary of the transformer is shorted with a small section of 1/4" copper tubing. This allows the Lp and Rs parameters to be measured.

inductance and resistance are neglected in further simulations due to low values.

4.1.4 Quality Factor of RLC circuit

The quality factor Q of the RLC circuit can be calculated using equation (3.11). The results are shown in Table 4.3. The no-workpiece result has the highest Q since there is no reflected resistance from a workpiece. The only resistance in the circuit is the 1/4" copper pipe and the ESR of the capacitor bank. All workpieces have a Q over 10 except 1006 steel.

Workpiece Material	Q Factor
No Workpiece	64.1
6061 Aluminum	40.8
304 Stainless Steel	22.1
1006 Steel	4.3

Table 4.3
Quality Factors of RLC Circuit

4.1.5 LC Tank Circuit Measurements

The LC tank circuit with the transformer was constructed in Figure 4.8. The calculated values and final circuit shown in Figure 4.9 were compared with the physical circuit. A Hioki 3532-50 LCR meter was used to measure impedance sweeping from 1-30kHz using 745 linear points. The kelvin probes are connected across the secondary of the transformer. The measured result is compared to the calculated result in Figure 4.10 for an unloaded work coil. The theoretical model closely matches the physical construction aside from non-linearities at the anti-resonant frequency, and the resonant points shifting due to differences in LC measurements.

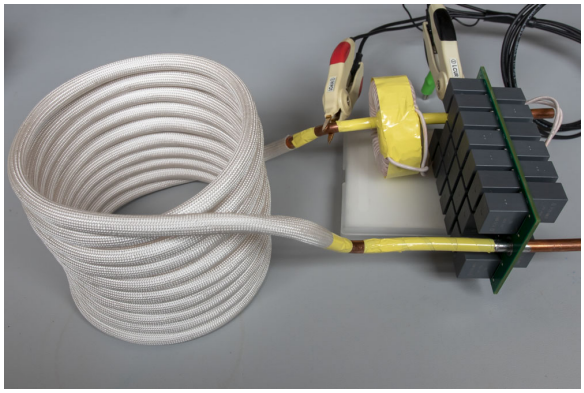

Figure 4.8: The RLC tank circuit is constructed and the impedance is measured from 1-30kHz across the secondary of the transformer.

A 2x4"(50.8x101.6mm) aluminum workpiece was placed in the workcoil and measured using the same technique. The calculated parameters are used from Table 4.2. From Figure 4.11, there is a significant difference between the calculated and FEA result.

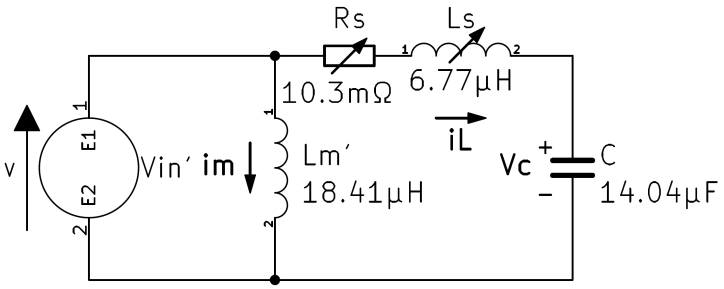

Figure 4.9: The previously calculated parameters are added to the theoretical model of the RLC tank circuit. *Rs* and *Ls* are varied based on the results of the FE analysis.

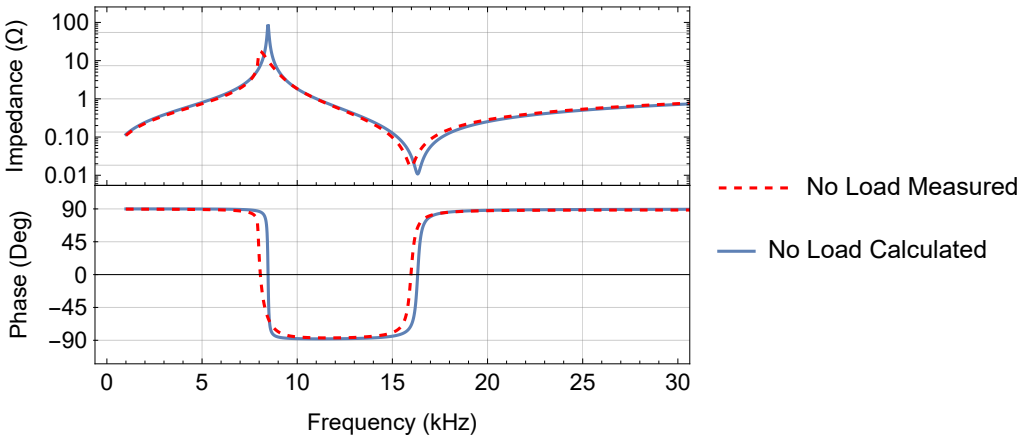

Figure 4.10: Impedance and phase are measured on an open workcoil from 1-30kHz. Results are compared to the theoretical model impedance and phase.

The measured resonant frequency occurs at approximately 16.97kHz while the calculated result is 17.84kHz. This is a difference of 4.99%. The difference is likely due to the test current for the Hioki LCR meter being under 90mA, while the FEA result was measured at 100Apk.

A bode plot of all the workpieces is shown in Figure 4.12. The gain represents the voltage to current gain of the combined mutual inductance and RLC circuit. The stainless steel and aluminum workpieces are similar in gain. The steel workpiece has

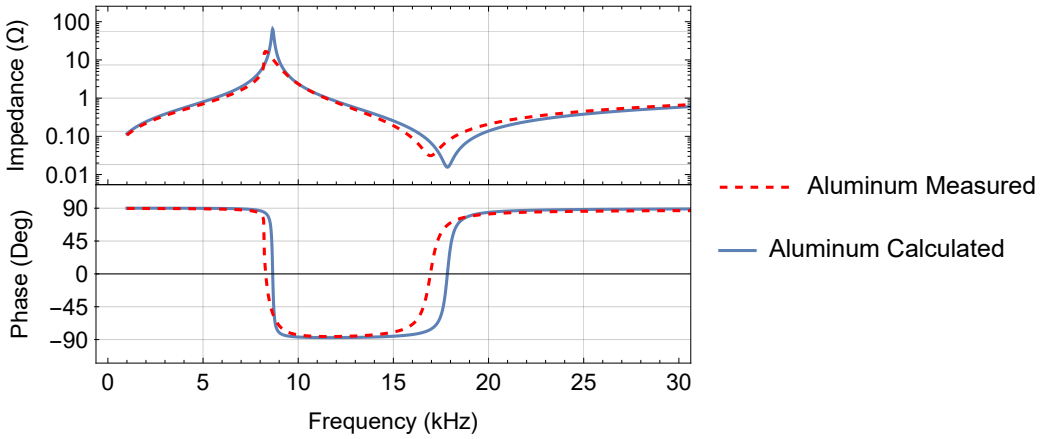

Figure 4.11: Impedance and phase are measured on a workcoil with the aluminum workpiece from 1-30kHz. The measured resonant frequency is significantly lower than the calculated results with a difference of 4.99%.

a high dampening effect due to low Q factor that substantially reduces the gain. The phase also does not reach 90° between the resonant and anti-resonant peaks for the steel workpiece.

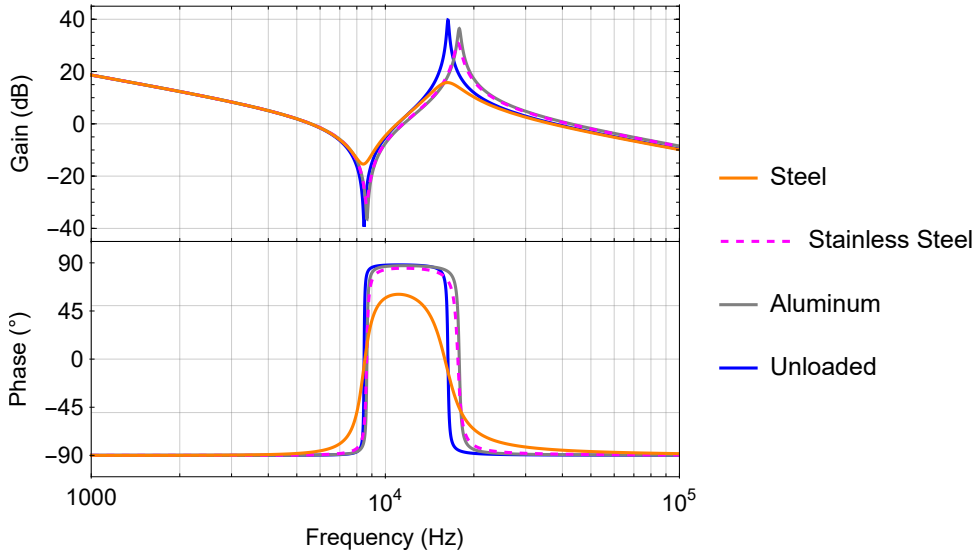

Figure 4.12: A plot of voltage to current gain and phase for the various workpieces shows steel having the highest damping effect leading to a reduced gain compared to the other workpieces. Stainless steel and aluminum have similar gains over frequency.

Chapter 5

Results

5.1 Nyquist Analysis

Nyquist analysis was performed for all workpieces in Table 4.2. The current of the series RLC circuit is used for A combined plot is shown in Figure 5.1. A table of results is available in Table 5.1. An unloaded workpiece has the largest estimated current at 487.5Apk or 344.7Arms at 16.33kHz. The current sits right below the rated current of the capacitor bank. This is due to the low resistance presented at the resonant frequency. The second highest current is the aluminum workpiece at 236.0Arms. Stainless steel has an RMS current of 124.4Arms. Steel has the highest resistance at the resonant frequency leading to an estimated current of 21.7Arms.

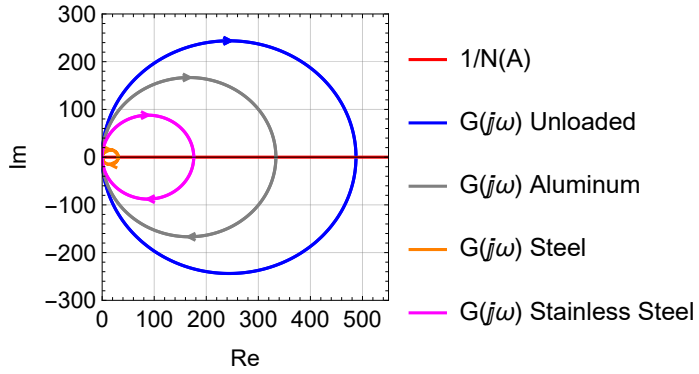

Figure 5.1: A Nyquist plot graphically showing solutions of the $G(j\omega) = 1/N(A)$ equation for all the workpieces. Limit cycles are predicted at the points of intersection. The real axis is the peak real current of the RLC tank circuit. The imaginary axis is the peak reactive current.

Workpiece Material	Peak Current (Apk)	RMS Current (Arms)	Frequency (kHz)
No Workpiece	487.5	344.7	16.33
6061 Aluminum	333.7	236.0	17.84
304 Stainless Steel	175.9	124.4	17.65
1006 Steel	30.66	21.7	16.10

Table 5.1
Currents at the Resonant Frequency for Workpieces Predicted from Nyquist Analysis

5.2 Simulation

The state equations in (3.4.1) were numerically solved using Mathematica 13.1. The complete code is available in Appendix A. u is replaced with the non-linear relay function (3.26). The transformer secondary voltage is $\pm 120\sqrt{2}/43$V or ± 3.94V if a 120V rectified source is connected as the bus voltage feeding the H-bridge.

5.2.1 Open Workcoil to Workcoil with Aluminum Workpiece

The simulation starts with an open workcoil. At t=0.01s, an aluminum workpiece is placed in the workcoil. This is accomplished by changing the inductance and resistance values of the workcoil using Table 4.2. All the states start at zero. The start-up waveform is shown in Figure 5.2. u[t] is the output voltage from the transformer secondary, x_2[t] is the current flowing through the inductor of the workcoil series RLC circuit. Positive feedback is occurring with the input voltage enhancing the current through the RLC circuit. The switching is happening at zero current.

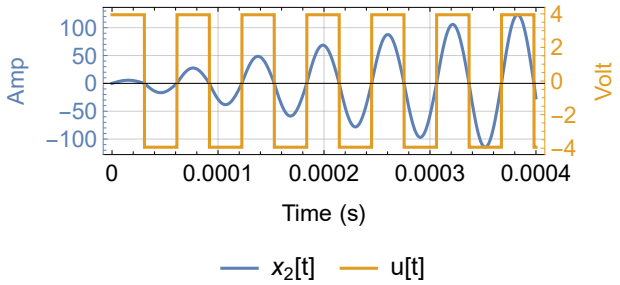

Figure 5.2: Startup of an open workcoil is simulated. A voltage of 3.94V is applied to the RLC circuit matching the polarity of the feedback current.

Figure 5.3 shows the steady-state operation of the open workcoil before 0.01s. The Nyquist analysis estimated the current at 487.5Apk. This is a difference of only 0.05%. When the aluminum workpiece is added at 0.01s, the switching frequency increases, and the current slowly reduces to 333.7Apk. The Nyquist analysis predicted an identical current of 333.7Apk.

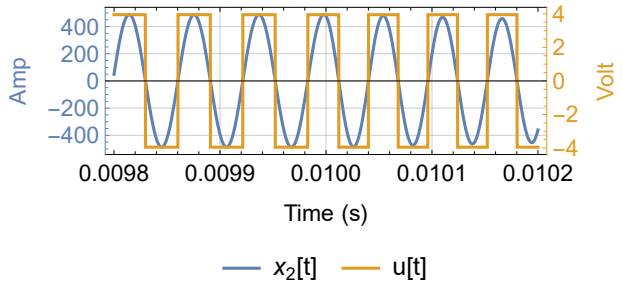

Figure 5.3: Before 0.01s, the open workcoil is operated at steady-state. The aluminum workpiece is added to the workcoil at 0.01s modifying the series inductance and resistance. This starts to reduce the current through the circuit.

From Figure 5.4, the open workcoil causes a voltage of 338Vpk across the capacitor bank. This exceeds the specification of 250Vdc. Therefore the workcoil cannot be operated with an open workcoil in a physical build at the maximum bus voltage. When the aluminum workpiece is inserted the voltage drops to 212Vpk.

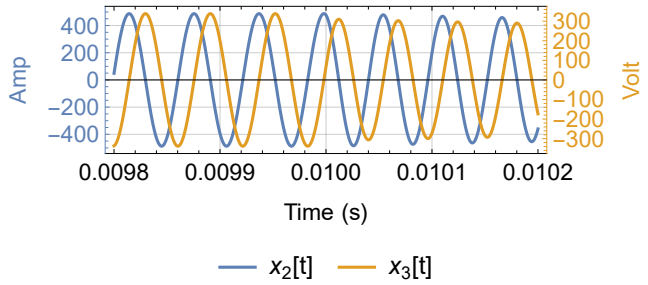

Figure 5.4: Adding the aluminum workpiece at 0.01s results in a reduction in voltage across the series capacitor.

Figure 5.5 looks at the I^2R power dissipation of the circuit. The open workcoil power is 2447Wpk, 1212Wavg. When the aluminum workpiece is inserted, the power drops to 1677Wpk or 837.6Wavg. When the workpiece is inserted, the power spikes to 3.5kW due to the increased resistance. The current drops to a new steady state as a

result. The stored energy in the RLC circuit shows a reduction in stored energy from 800mJ to 425mJ.

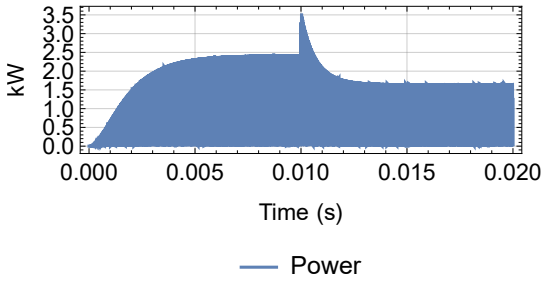

Figure 5.5: The power with an open workcoil is 1212Wavg. The aluminum workpiece is added to the workcoil at 0.01s. The power of a workcoil with aluminum is 837.6Wavg.

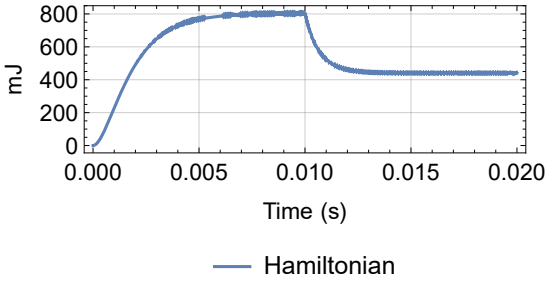

Figure 5.6: The Hamiltonian of the series RLC tank circuit shows a reduction in stored energy as a result of adding the aluminum workpiece at 0.01s.

The simulated frequency is found cycle-by-cycle using

$$f = \frac{1}{2(t_n - t_{n-1})} \tag{5.1}$$

where t_n is the time when the RLC current crosses 0, t_{n-1} is the previous time the current crossed zero. Figure 5.7 shows the simulated frequency of operation

compared to the value found from Nyquist analysis. The calculated value matches the simulated value with an open workcoil and with an aluminum workpiece. With an open workcoil the calculated value is 16.329kHz, and the simulated frequency is 16.328kHz, a difference of 0.006%. When an aluminum workpiece is added, the calculated resonant frequency is 17.839kHz, the simulated frequency is 17.838kHz, a difference of 0.006%.

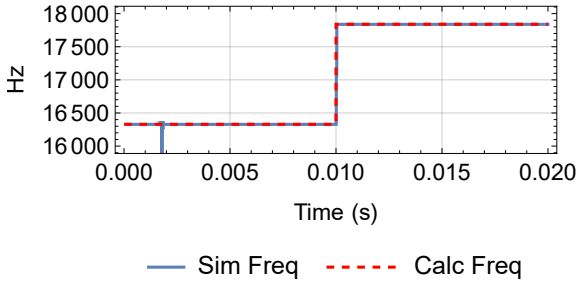

Figure 5.7: The frequency changes from 16.33kHz with an open workcoil to 17.84kHz at 0.01s when an aluminum workpiece is added.

5.2.2 Workcoil with Steel Workpiece

The induction heater with a 1006 steel workpiece inside the workcoil at start-up is simulated. Figure 5.8 shows the start-up waveform. It reaches a steady-state current of 30.67Apk in 2ms. This is a 0.12% difference from the estimated value from the Nyquist analysis. The voltage across the capacitor is 21.7V from Figure 5.9.

Figure 5.10 shows the power is only 150Wpk or 76.8Wavg. A different transformer and capacitor bank design is needed to heat steel effectively due to the high reflected

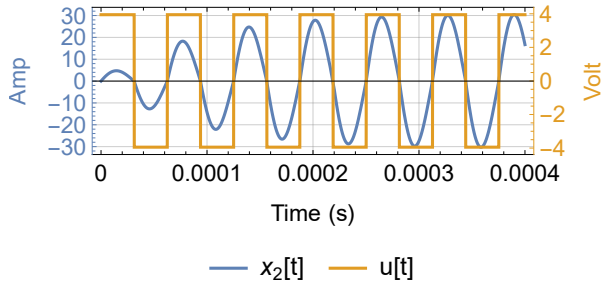

Figure 5.8: Steel workpiece series RLC current and applied secondary voltage waveform at startup.

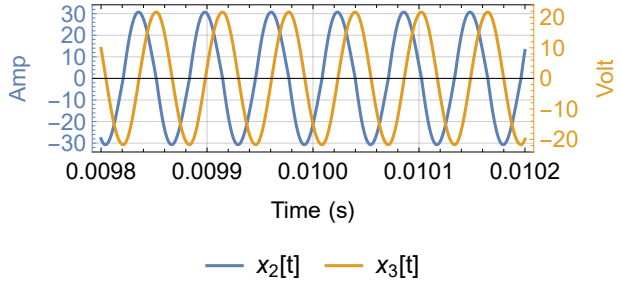

Figure 5.9: Steel workpiece RLC current compared to capacitor bank voltage.

resistance.

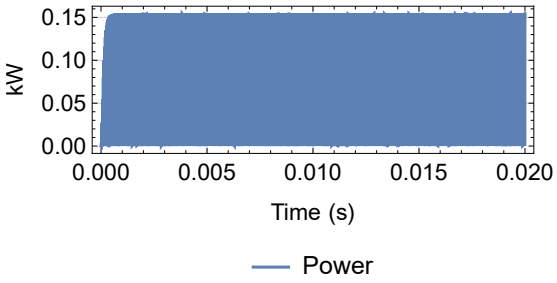

Figure 5.10: Steel workpiece power dissipated in series RLC resistance.

Due to the high reflected resistance, the quality factor is only 4.28 for the workcoil. This leads to a difference between the ideal resonant equation (3.4) and the exact resonant equation (3.9). The difference of 0.68% is seen in the simulation shown in

Figure 5.11.

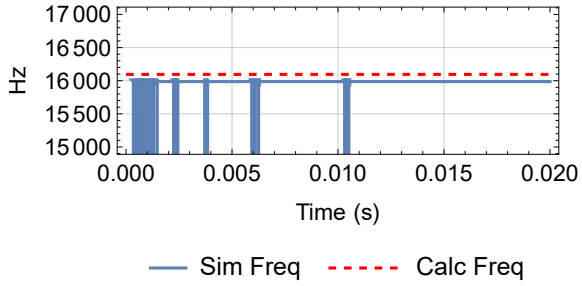

Figure 5.11: Steel workpiece frequency of operation simulation difference compared to calculated.

5.2.3 Results Compared to Nyquist Analysis

Two tables of results summarize the current and resonant frequency estimated from Nyquist analysis compared to the simulated results for all workpiece materials. All differences were under 1%. The highest difference in workcoil current is with the steel workpiece of 0.13% shown in Table 5.2. The highest difference in resonant frequency is with the steel workpiece in Table 5.3. The difference of 0.68% matches the difference found by using the ideal calculation compared to the exact calculation. The Nyquist analysis does not take into account the slight difference in resonant frequency due to the low quality factor.

Workpiece Material	Nyquist I (Apk)	Simulated I (Apk)	Diff. (%)
No Workpiece	487.50	487.29	0.04
6061 Aluminum	333.70	333.68	0.01
304 Stainless Steel	175.90	175.87	0.02
1006 Steel	30.66	30.70	0.13

Table 5.2
Nyquist Compared to Simulation for Workcoil Current

Workpiece Material	Nyquist Freq. (kHz)	Simulated Freq. (kHz)	Diff. (%)
No Workpiece	16.33	16.33	0.00
6061 Aluminum	17.84	17.84	0.01
304 Stainless Steel	17.65	17.65	0.02
1006 Steel	16.10	15.99	0.68

Table 5.3
Nyquist Compared to Simulation for Resonant Frequency

5.3 Hardware Implementation

A hardware circuit was developed to verify the findings of limit cycles in the simulation and Nyquist analysis. An aluminum workpiece was used in the physical tests. Deadtime was added to prevent shoot-through which is when both the top and bottom transistors in the H-bridge turn on at once leading to a high current condition. The complete schematic is available in Appendix B.

5.3.1 H-Bridge

The H-bridge circuit uses four n-channel MOSFETs to transform a bus voltage into a voltage alternating between +VBUS and -VBUS. The circuit is shown in Figure 5.12. This voltage is supplied across the transformer created in section 4.1.3. The secondary of the transformer is the series RLC workcoil circuit. FQA40N025 MOSFETs were chosen due to their 250Vds voltage and low rds-on of 70mΩ. The current capability is 40 amps continuous. The package was also a consideration being mounted on a heatsink accepting TO-247 packages. C40-058-VE heatsinks were chosen for the MOSFETs because two heatsinks could accept four MOSFETs. Two heatsinks together also support a 40mm fan. The 10kΩ resistors from gate to source prevent the MOSFET gate from floating if the pulse transformer were to get disconnected. The series 100Ω resistors prevent the capacitance of the MOSFET gate from charging up too fast. This leads to excessive ringing on the gate. IT143 pulse transformers were chosen due to their large volt-microsecond product of 800Vμs. The volt-microseconds needed for an aluminum workpiece is 15V*1/17.84kHz=840.8Vμs. This exceeds the specification by 4.97%. A custom pulse transformer with a larger Vμs product or a different gate driving technique would be ideal. One pulse transformer with two secondaries is used for each half of the bridge. The pulse transformer polarities are arranged to turn on either Q1 and Q5 or Q2 and Q4. Series capacitors C12, C13, and C15 are added to transformer T5 to prevent flux-walk saturation caused by a DC

component across the primary.

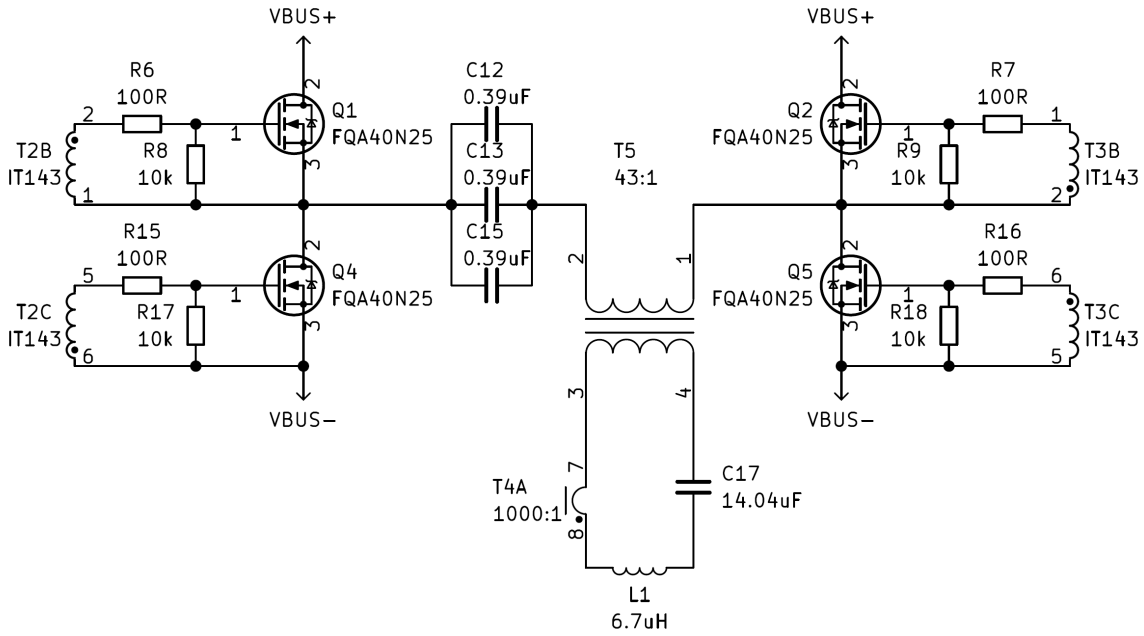

Figure 5.12: H-bridge circuit consists of four n-channel MOSFET switches configured in an "H" pattern. The 43:1 transformer and series capacitor are in-between the two switch stacks.

5.3.2 Voltage Supply

The bus voltage is supplied from a 120V 60Hz outlet. This is fed through a variac to manually control the power. The output from the variac is passed through a bridge rectifier and a small set of filtering capacitors. There is enough capacitance to create a steady voltage to aid in startup of the circuit. When the current increases, the bus voltage shifts to a rectified sinewave shape of the line voltage. This creates a high power factor for the induction heater.

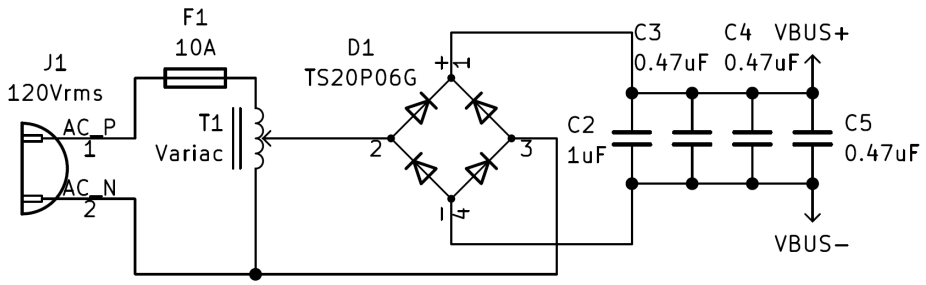

Figure 5.13: The 120Vrms line is varied using a variac. The output of the variac is full-bridge rectified.

5.3.3 Control and Gate Driver

To prevent shoot-through of each half-bridge, dead-time is introduced. The main control portion consists of two comparators. Two DC voltages, PH and PL, are generated by the voltage dividers formed by R2, RV1A, R4, and R19, RV1B, and R20. One voltage is positive while the other is negative. A dual-gang potentiometer, RV1, controls the magnitude of the voltages from zero. These reference voltages are fed into the comparators. A 1000:1 current transformer is placed around the secondary in Figure 5.12 as T4A. This is the current feedback mechanism. The secondary of the current transformer is converted to a voltage with R10 and R13. RV2 and C14 form a phase adjustment network and low pass filter.

The LM393 dual comparator IC is used for the comparators. It was chosen due to the high voltage range of 36V maximum and open-collector outputs. It is powered by ±15V supplies. The logic output of the comparators is ground as a high signal and -15V as a low signal. Comparator U1A handles the positive current. It compares

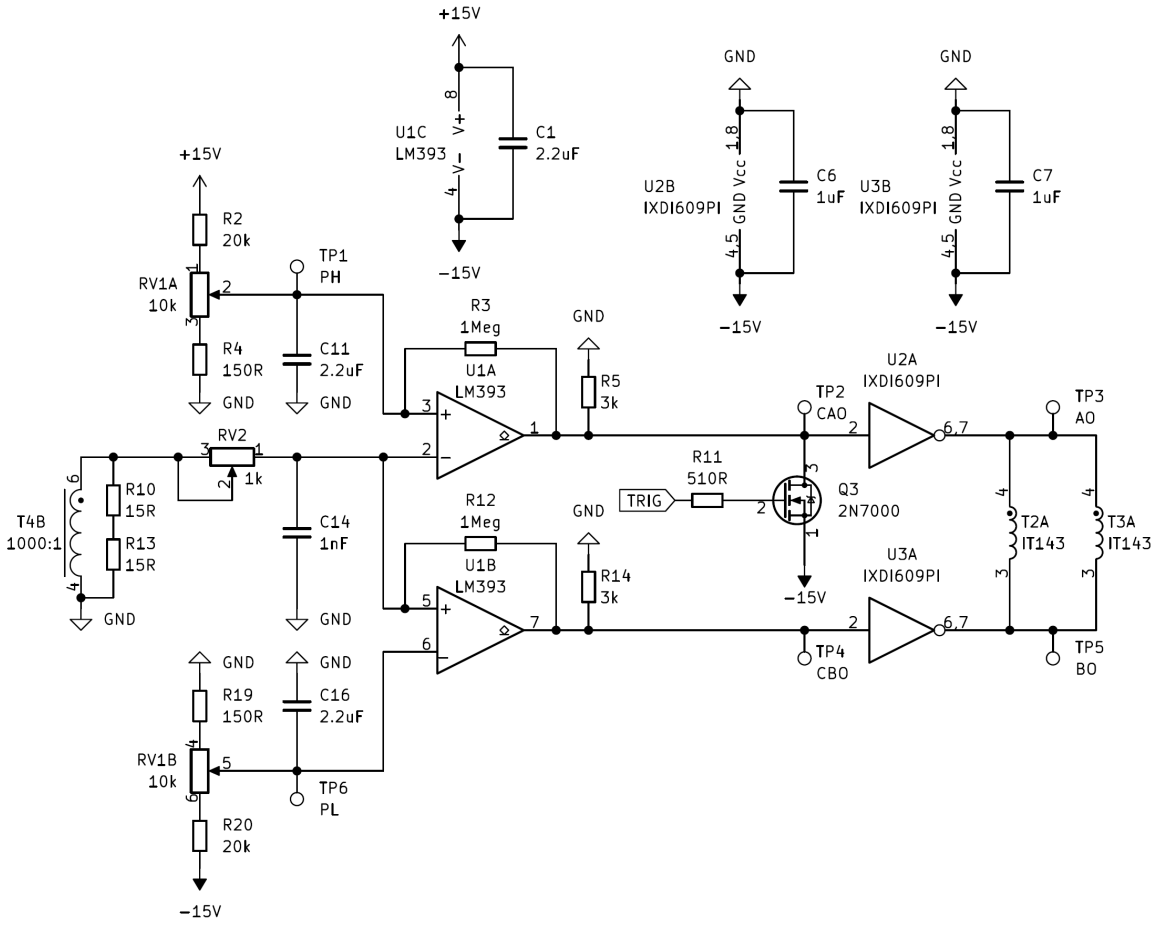

Figure 5.14: The control circuit consists of two main comparators which actuate the switches from the polarity of the voltage from the current transformer. Q3 starts the oscillation.

the current signal to the positive reference. If the current signal is a higher voltage than the reference, the output, CAO, goes low. R3 and R12 provide a small amount of hysteresis. Comparator U1B handles the negative current. If the current signal is lower than the reference, the output, CBO, goes low. When both outputs are high, no current flows through the pulse transformers. If the current goes above or below the threshold set by the voltage references, only one comparator output goes low causing current to flow through the pulse transformers. The IXDI609PI IC is a 9Apk low-side

MOSFET driver with Schmitt trigger input. This provides current amplification of the comparator output to drive two IT143 pulse transformers in parallel. Current can only flow one direction at a time through the pulse transformers preventing all transistors from turning on at once. The completed control and H-bridge module are shown in Figure 5.15.

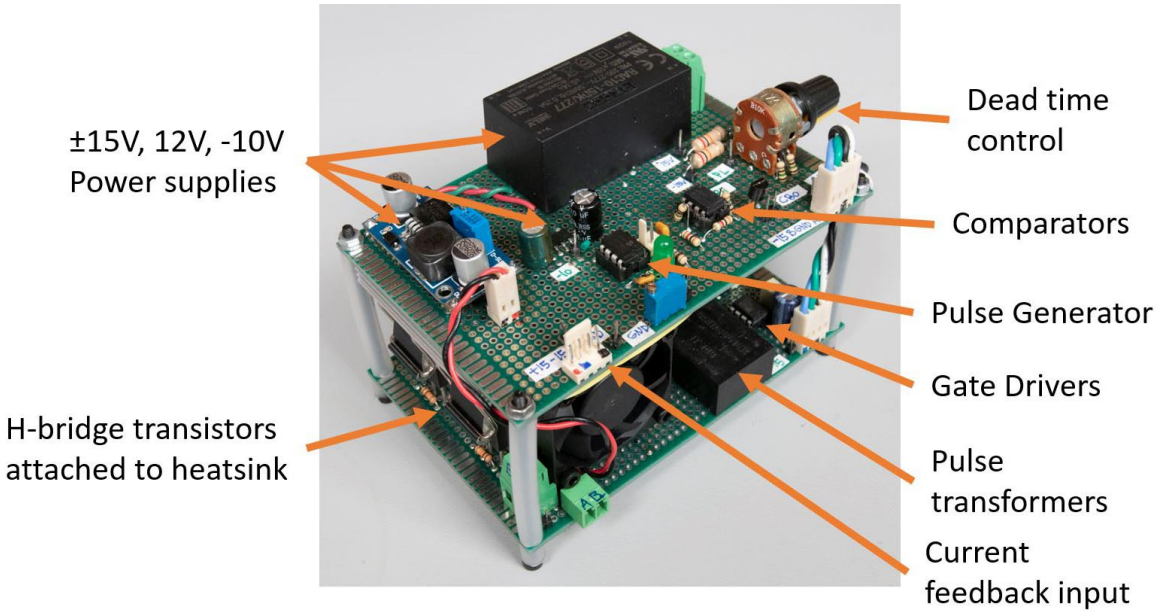

Figure 5.15: The control and power section are constructed in one module.

The circuit is not self-starting due to the addition of dead time. To start the circuit, Q3 brings down the CAO node to -15V simulating positive current in the circuit in Figure 5.14. Q3 is controlled by a PIC12F1572 microcontroller, Figure 5.16, which outputs a 1/4 wavelength pulse of 15.3μs when button SW1 is pressed. Debouncing prevents multiple triggers. The microcontroller code is available in Appendix C.

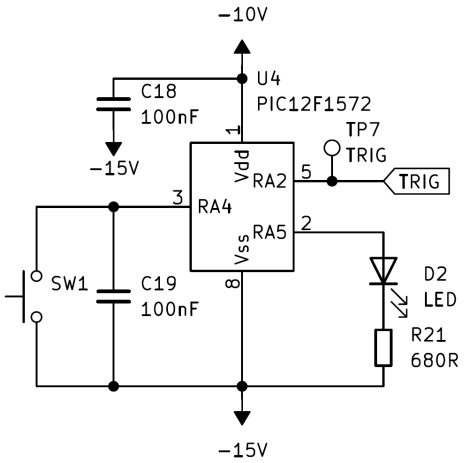

Figure 5.16: The pulse generator is a microcontroller that outputs a 15.3μs pulse.

5.3.4 Current Transformer

The number of winds of the current transformer T4 is found using

$$Ns = \frac{Ip \cdot Np \cdot R}{Vo} \tag{5.2}$$

where Ns is the number of secondary winds, Np is the number of primary winds, Ip is the primary current, R is the load resistor value, Vo is the output/secondary voltage. With Np=1, Ip=350A, R=30Ω, Vo=10V, the number of winds is estimated to be 1050. The number of winds was rounded to 1000. 30 AWG enameled copper wire was used. The core part number is 77930A7 from Magnetic Inc. The completed transformer is shown in Figure 5.17.

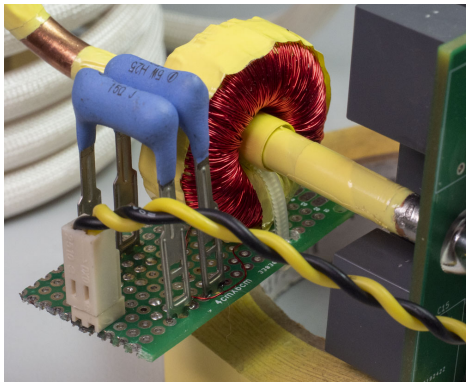

Figure 5.17: 1000:1 current transformer is constructed from 30AWG wire. The load resistance is 30Ω.

5.3.5 Low Voltage Test Results

The circuit was initially tested using a bus voltage of 25V using a BK Precision 1685B DC lab power supply. An aluminum workpiece was placed in the workcoil. A 43:1 T4 current transformer was used for this test. The primary current was measured with a Tektronix AM503 current probe amplifier paired with a Tektronix A6302 current probe. The voltage output across the H-bridge was measured with a GW Instek GDP-025 differential probe. An MSO5074 oscilloscope captured the signals including the comparator outputs, CAO, and CBO, with 10x probes. The captured waveforms are shown in Figure 5.18. The comparator outputs alternate between ground and -15V with the sign of the current feedback supplied by the current transformer. This actuates the MOSFET switches leading to a ±25V output across the H-bridge. The primary current is measured at one amp peak. The frequency was measured to be 17.14kHz. This is a 4.00% difference from the Nyquist and simulation results.

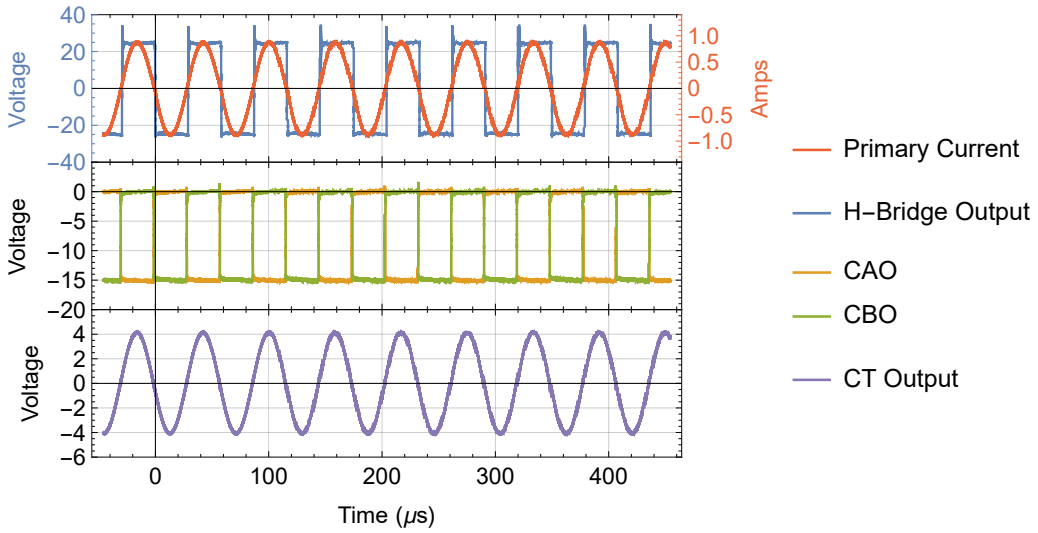

Figure 5.18: Low voltage steady-state test waveforms consisting of primary current, H-bridge differential output, comparator signals, and CT voltage

The start-up waveform is shown in Figure 5.19. The first negative pulse for the CAO signal is generated by the microcontroller. This starts the comparator circuit which allows the primary current to increase.

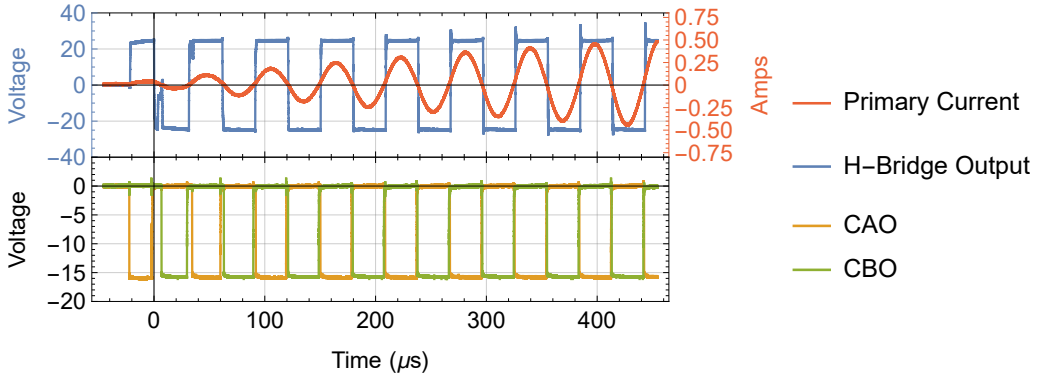

Figure 5.19: Low voltage startup test waveforms consisting of primary current, H-bridge differential output, and comparator signals.

5.3.6 Line Voltage Test Results

The induction heater is connected to a 120Vrms line in this test using the circuit in Figure 5.13. This allowed the heater to operate at the designed peak voltage of 170V. A Hioki 3332 power meter was connected to the output of the variac. A Yokogawa WT210 power meter was connected to the output of the H-bridge. This allowed the efficiency and input power factor of the converter to be measured. The workcoil was water-cooled due to the resistance of the copper dissipating significant power at high current. 1/4" plastic lines were connected to each end of the 1/4" copper tubing using compression fittings. A diaphragm pump circulated tap water through the copper tubing cooling the workcoil. Polyimide tape is applied to the top of the aluminum workpiece to correct emissivity for thermal imaging. The test setup is shown in Figure 5.20.

The circuit was started with a line voltage of 70-110Vrms to prevent saturation of the T5 transformer. Due to excessive inrush current, the circuit could not be started above 110Vrms line voltage without saturation. After the circuit starts oscillating, the line voltage could be brought up to 120Vrms. The primary current of T5 and the bus voltage were captured with a line voltage of 120Vrms shown in Figure 5.21. The bus voltage varies from 0-170V following the 60Hz line frequency. The primary current ranged from 1-6.5Apk. The input power at 120Vrms line voltage was 383.9Wrms.

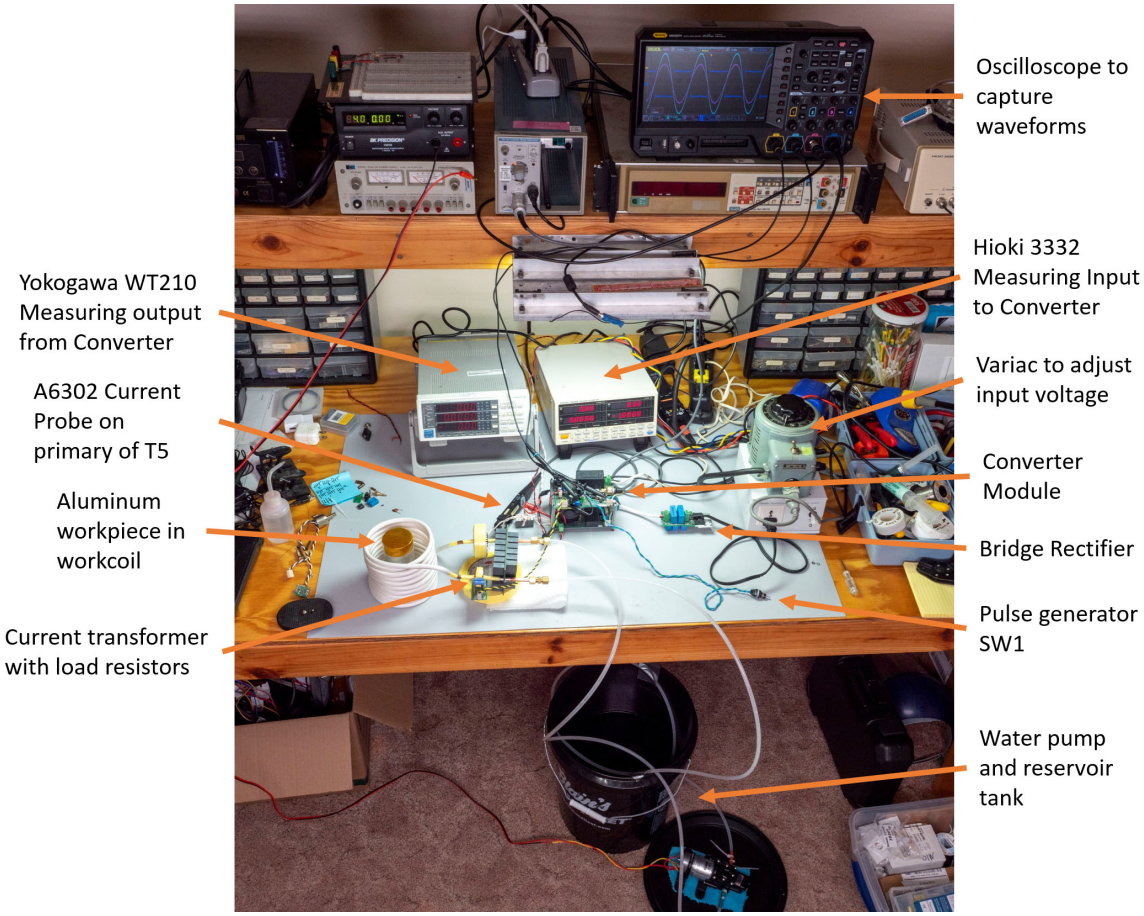

Figure 5.20: Workbench setup for line voltage test on induction heater.

The output power from the converter is 329.7Wrms. This is an efficiency of 85.9%. The power factor was measured to be 0.972. The simulation was re-run with a bus voltage of 120Vdc. The power from the simulation is 418.8Wrms with an aluminum workpiece. The measured power is 23.8% less than the simulated power. A thermal image was captured of the circuit in Figure 5.22 using a Seek Thermal ShotPRO. The workpiece reached 136˚F and rising before the circuit was switched off to prevent the workpiece from overheating. More thermal insulation and a foundry environment are needed to heat the workpiece to a higher temperature.

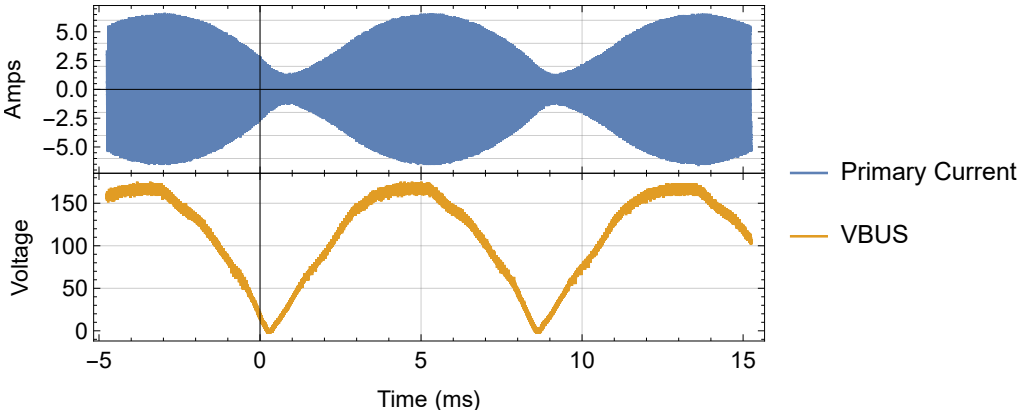

Figure 5.21: Line voltage test waveforms of primary current and VBUS voltage.

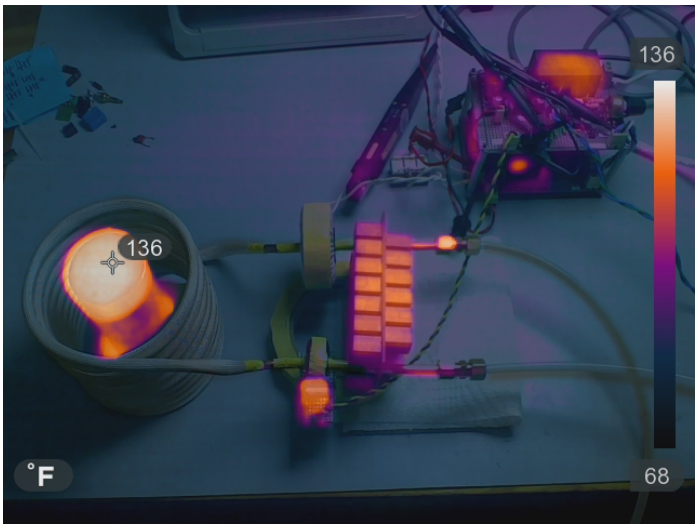

Figure 5.22: Thermal image of the induction heater with an aluminum workpiece in workcoil.

Chapter 6

Conclusion and Future Work

6.1 Conclusion

Nyquist analysis of the non-linear relay control system was found to be accurate for quality factors above 10. It accurately predicted the existence of limit cycles for a series RLC circuit. For Q factors near 5, for example, the 1006 steel workpiece, Nyquist analysis is less accurate at predicting the frequency of resonance. For current flowing through the RLC circuit, Nyquist analysis has a higher accuracy for Q factors near 5 than frequency.

A hardware circuit was constructed and an aluminum workpiece was used in operation. The frequency was 4% different than Nyquist prediction. The captured waveforms from the experiment are comparable to the simulated results. The measured power was 23.8% less than the simulated result at the same RMS bus voltage.

6.2 Future Work

A constant power circuit is needed due to the variation of power using different workpieces. It would also reduce the power if the workcoil were to operate with no workpiece. The power was manually operated in the hardware circuit using a variac. The power can be adjusted also by the dead time of the control circuit. Increasing the dead time reduces the pulse width of the H-bridge circuit output. The current and power is reduced as a result. A high-side controller that can sense the voltage across the H-bridge and primary current would be able to adjust the dead time to meet a power requirement.

A BH curve saturation model of the T5 transformer would be helpful in solving the inrush current problem when starting the circuit over 110Vrms line voltage. Adding a series inductor to the input would help reduce this issue.

The workpiece temperature affects the reflected resistance and inductance. Steel for

example has a high relative permeability at room temperature. When steel approaches its Curie point, approximately 700°C, the relative permeability reduces to zero. This changes the resonant frequency. This applies only to magnetic materials. Including a temperature model for the steel workpiece would improve accuracy.

References

[1] Panchal, Santosh and Kulkarni, R.D. and Kumar Raja, M. and Nataraj, J., "Design, Simulation and Hardware Implementation of Soft Switching based Induction Heating System," in *2021 6th International Conference for Convergence in Technology (I2CT)*, pp. 1–7, 2021.

[2] Lucía, Oscar and Maussion, Pascal and Dede, Enrique J. and Burdío, José M., "Induction Heating Technology and Its Applications: Past Developments, Current Technology, and Future Challenges," *IEEE Transactions on Industrial Electronics*, vol. 61, no. 5, pp. 2509–2520, 2014.

[3] Vishnuram, Pradeep and Ramachandiran, Gunabalan and Ramasamy, Sridhar and Dayalan, Suchitra, "A Comprehensive Overview of Power Converter Topologies for Induction Heating Applications," *International Transactions on Electrical Energy Systems*, vol. 30, no. 10, p. e12554, 2020.

[4] Kamli, M. and Yamamoto, S. and Abe, M., "A 50-150 kHz Half-Bridge Inverter

for Induction Heating Applications," *IEEE Transactions on Industrial Electronics*, vol. 43, no. 1, pp. 163–172, 1996.

[5] Grajales, L. and Lee, F.C., "Control System Design and Small-Signal Analysis of a Phase-Shift-Controlled Series-Resonant Inverter for Induction Heating," in *Proceedings of PESC '95 - Power Electronics Specialist Conference*, pp. 450–456 vol.1, 1995.

[6] Yeon, Jae-Eul and Cho, Kyu-Min and Kim, Hee-Jun, "A 3.6kW Single-Ended Resonant Inverter for Induction Heating Applications," in *2015 17th European Conference on Power Electronics and Applications (EPE'15 ECCE-Europe)*, pp. 1–7, 2015.

[7] Walter, Julio and Ceglia, Gerardo and Guzman, Victor and Gimenez, Maria, "Control Model of a Closed Loop Power-Controlled Series-Type Resonant Induction Heating System," in *2007 European Conference on Power Electronics and Applications*, pp. 1–8, 2007.

[8] Pavao, R.K. and Bisogno, F.E. and Seidel, A.R. and do Prado, R.N., "Self-Oscillating Electronic Ballast Design Based on the Point of View of Control System," in *Conference Record of the 2001 IEEE Industry Applications Conference. 36th IAS Annual Meeting (Cat. No.01CH37248)*, vol. 1, pp. 211–217 vol.1, 2001.

[9] Gokcek, C., "Tracking the Resonance Frequency of a Series RLC Circuit using a Phase Locked Loop," in *Proceedings of 2003 IEEE Conference on Control Applications, 2003. CCA 2003.*, vol. 1, pp. 609–613 vol.1, 2003.

[10] Julio Walter and Gerardo Ceglia, "Using Numerical Methods to Design and Control Heating Induction Systems," in *Advances in Induction and Microwave Heating of Mineral and Organic Materials* (S. Grundas, ed.), ch. 5, Rijeka: InteChOpen, 2011.

[11] Takau, Lisiate and Bodger, Pat, "Low Frequency Modelling of Induction Heaters using Series Equivalent Circuit, Transformer Equivalent Circuit and Finite Element Analysis," in *2013 Australasian Universities Power Engineering Conference (AUPEC)*, pp. 1–6, 2013.

[12] Garcia, S. and Medina, A. and Perez, C., "A State Space Single-Phase Transformer Model Incorporating Nonlinear Phenomena of Magnetic Saturation and Hysteresis for Transient and Periodic Steady-State Analysis," in *2000 Power Engineering Society Summer Meeting (Cat. No.00CH37134)*, vol. 4, pp. 2417–2421 vol. 4, 2000.

[13] J.-J. Slotine and W. Li, *Applied Nonlinear Control*. New Jersey: Prentice-Hall, Inc., 1991.

[14] W. Hayt and J. Buck, *Engineering Electromagnetics*. New York, NY: McGraw-Hill, 2012.

[15] Meeker, David, "Finite Element Method Magnetics Version 4.2 User's Manual," May 2020.

[16] Kemet, "R76, Double Metallized Polypropylene Film, Radial, DC and Pulse Applications Datasheet," 2022.

Appendix A

Nyquist Analysis and Simulation Code

NyquistAnalysisV4

In[1]:=
```
Clear["Global`*"]
SetDirectory[NotebookDirectory[]];
SetOptions[SelectedNotebook[],
  PrintingStyleEnvironment → "Printout", ShowSyntaxStyles → True];
MyPlot[x_, ti_, tf_, xlabel_, ylabel_, style_, points_, bottomSpace_, led_] :=
 Plot[x, {t, ti, tf}, Exclusions → None, PlotRange → Full, AspectRatio → 1 / 3,
  ImageSize → 350, PlotStyle → style, Frame → True, PlotPoints → points,
  FrameLabel → {xlabel, ylabel}, GridLines → Automatic, BaseStyle → {"Times", 12},
  ImagePadding → {{60, 60}, {bottomSpace, 5}}, PlotLegends → led]
PDiff[v1_, v2_] := Abs[v1 - v2] / ((v1 + v2) / 2) 100
ResCalc[ls_, rs_, c_, cEsr_] := {
  qFactor = Sqrt[ls / c] / (rs + cEsr),
  ζ = 1 / (2 qFactor),
  ω_ni = 1 / Sqrt[ls c],
  ω_ri = ω_ni Sqrt[1 - ζ^2],
  fResApprox = ω_ni / (2 Pi)} (*Q-quality factor,ζ-damping ratio,
ω_ni-resonant freq approx rad/s,ω_ri-resonant freq exact rad/s,
fResApprox-resonant frequency approx Hz*)
```

RLC Circuit Relay Non-linearity Describing Function Analysis

State equation and parameters

In[7]:=
```
param = <|capC → 14.04 × 10^-6,
    capEsr → 0.000521, lm → 34.01 × 10^-3 / 43^2, busVolt → 120 Sqrt[2]|>;
unloadedLR = <|ls → 6.76668 × 10^-6, rs → 10.3072 × 10^-3|>;
alumLR = <|ls → 5.66925 × 10^-6, rs → 15.0602 × 10^-3|>;
ssLR = <|ls → 5.79067 × 10^-6, rs → 28.5739 × 10^-3|>;
steelLR = <|ls → 6.96401 × 10^-6, rs → 163.881 × 10^-3|>;
```

In[12]:=
```
states = {x1[t], x2[t], x3[t]};
inputs = {u[t]};
eq1 = 1 / lm u[t];
eq2 = 1 / ls (u[t] - x2[t] rs - x3[t]);
eq3 = 1 / capC (x2[t]);
ode = {
    x1'[t] == eq1,
    x2'[t] == eq2,
    x3'[t] == eq3
  };
% // MatrixForm
```

Out[18]//MatrixForm=

$$\begin{pmatrix} x_1'[t] == \frac{u[t]}{lm} \\ x_2'[t] == \frac{u[t]-rs\,x_2[t]-x_3[t]}{ls} \\ x_3'[t] == \frac{x_2[t]}{capC} \end{pmatrix}$$

Resonant frequency, Q calculation

In[19]:=
```
ResCalc[ls, rs, capC, capEsr] /. unloadedLR /. param
ResCalc[ls, rs, capC, capEsr] /. alumLR /. param
ResCalc[ls, rs, capC, capEsr] /. ssLR /. param
ResCalc[ls, rs, capC, capEsr] /. steelLR /. param
```

Out[19]=
```
{64.1133, 0.0077987, 102596., 102592., 16328.6}
```

Out[20]=
```
{40.7829, 0.01226, 112087., 112078., 17839.1}
```

Out[21]=
```
{22.0731, 0.022652, 110905., 110877., 17651.1}
```

Out[22]=
```
{4.2839, 0.116716, 101132., 100440., 16095.6}
```

Transfer function

In[23]:=
```
xMat = {{x1[t]}, {x2[t]}, {x3[t]}};
aMat = D[{eq1, eq2, eq3}, {states}];
bMat = D[{eq1, eq2, eq3}, {inputs}];
cMat = {{1, 1, 0}};
cMatRes = {{0, 1, 0}};
cMatAntiRes = {{1, 0, 0}};
ssModel = StateSpaceModel[{aMat, bMat, cMat}];
ssModelRes = StateSpaceModel[{aMat, bMat, cMatRes}];
ssModelAntiRes = StateSpaceModel[{aMat, bMat, cMatAntiRes}];
tfModel = TransferFunctionModel[ssModel, s] // FullSimplify
tfModelRes  = TransferFunctionModel[ssModelRes, s] // FullSimplify
tfModelAntiRes = TransferFunctionModel[ssModelAntiRes, s] // FullSimplify
tfModeljwSym = cMatRes.Inverse[j ω IdentityMatrix[3] - aMat].bMat // First;
tfModeljw = tfModeljwSym // FullSimplify
```

Out[32]=

$$\left(\frac{1+\text{capC}\,s\,(rs+(lm+ls)\,s)}{lm\,s\,(1+\text{capC}\,s\,(rs+ls\,s))}\right)_{\mathcal{T}}$$

Out[33]=

$$\left(\frac{\text{capC}\,s^2}{s\,(1+\text{capC}\,s\,(rs+ls\,s))}\right)_{\mathcal{T}}$$

Out[34]=

$$\left(\frac{1+\text{capC}\,s\,(rs+ls\,s)}{lm\,s\,(1+\text{capC}\,s\,(rs+ls\,s))}\right)_{\mathcal{T}}$$

Out[36]=

$$\left\{\frac{i\,\text{capC}\,\omega}{1+\text{capC}\,\omega\,(i\,rs-ls\,\omega)}\right\}$$

In[37]:=
```
(*qFactorSym= Sqrt[ls/c]/(rs)
  ζSym=1/(2qFactorSym)
   ωnSym=1/Sqrt[ls c]
    ωrSym=ωnSymSqrt[1-ζSym^2]//FullSimplify*)
```

Bode plots

In[38]:=
```
minFreq = 1 × 10^3;
maxFreq = 1 × 10^5;
minMult = 3;
maxMult = 5;
minDeg = -110;
maxDeg = 110;
minGain = -45;
maxGain = 45;
aspRatio = 0.4;
ResourceFunction["PlotGrid"][{
  {Show[{BodePlot[tfModel[2 Pi s] /. unloadedLR /. param, {minFreq, maxFreq},
      GridLines → Automatic, ImageSize → 200, AspectRatio → aspRatio,
      BaseStyle → {"Times", 12}, PlotLayout → "Magnitude", PlotStyle → Blue,
      PlotLegends → {"Unloaded"}, PlotRange → {{minMult, maxMult}, {minGain, maxGain}}],
     BodePlot[tfModel[2 Pi s] /. alumLR /. param, {minFreq, maxFreq},
      PlotLayout → "Magnitude", PlotStyle → Gray, PlotLegends → {"Aluminum"}],
     BodePlot[tfModel[2 Pi s] /. ssLR /. param, {minFreq, maxFreq}, PlotLayout → "Magnitude",
      PlotStyle → {Dashed, Magenta}, PlotLegends → {"Stainless Steel"}],
     BodePlot[tfModel[2 Pi s] /. steelLR /. param, {minFreq, maxFreq},
      PlotLayout → "Magnitude", PlotStyle → Orange, PlotLegends → {"Steel"}]
    }, Frame → True, FrameLabel → {None, "Gain (dB)"}, FrameStyle → Black]
  },
  {Show[{BodePlot[tfModel[2 Pi s] /. unloadedLR /. param,
      {minFreq, maxFreq}, GridLines → Automatic, ImageSize → 200,
      AspectRatio → aspRatio, BaseStyle → {"Times", 12}, PlotLayout → "Phase",
      PlotStyle → Blue, PlotRange → {{minMult, maxMult}, {minDeg, maxDeg}},
      FrameTicks → {{{-90, -45, 0, 45, 90}, None}, {Automatic, None}},
      GridLines → {Automatic, {-90, -45, 0, 45, 90}}],
     BodePlot[tfModel[2 Pi s] /. alumLR /. param, {minFreq, maxFreq}, PlotLayout → "Phase",
      PlotStyle → Gray, PlotRange → {{minMult, maxMult}, {minDeg, maxDeg}}],
     BodePlot[tfModel[2 Pi s] /. ssLR /. param, {minFreq, maxFreq}, PlotLayout → "Phase",
      PlotStyle → {Dashed, Magenta}, PlotRange → {{minMult, maxMult}, {minDeg, maxDeg}}],
     BodePlot[tfModel[2 Pi s] /. steelLR /. param, {minFreq, maxFreq}, PlotLayout → "Phase",
      PlotStyle → Orange, PlotRange → {{minMult, maxMult}, {minDeg, maxDeg}}]
    }, Frame → True, FrameLabel → {None, "Phase (°)"}, FrameStyle → Black]
  }
}, FrameLabel → {"Frequency (Hz)", None}, BaseStyle → {"Times", 12}]
```

Out[47]=

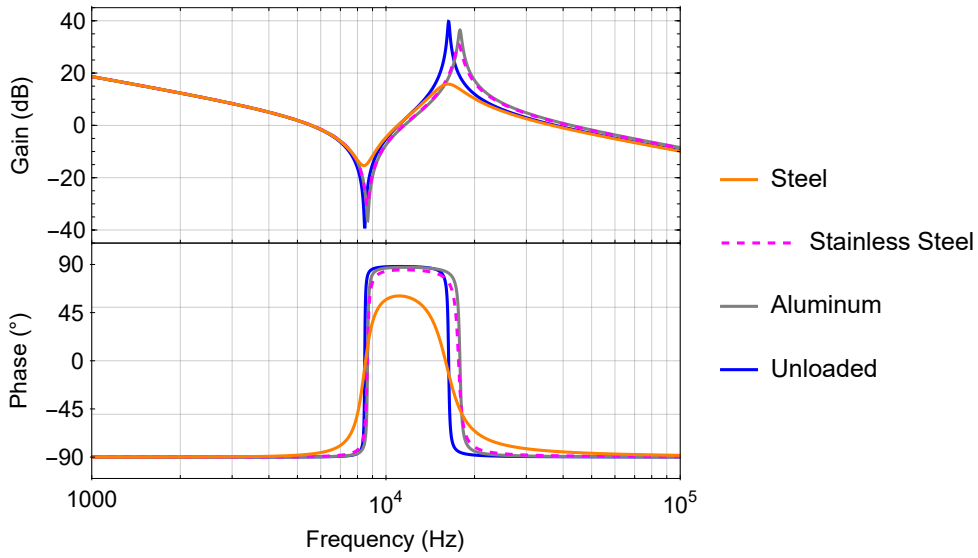
40
20
0
−20
−40
Gain (dB)
90
45
0
−45
−90
Phase (°)
1000
10^4
10^5
Frequency (Hz)
Steel
Stainless Steel
Aluminum
Unloaded

In[48]:=
```
minFreq = 1 × 10^3;
maxFreq = 1 × 10^5;
minMult = 3;
maxMult = 5;
minDeg = -110;
maxDeg = 110;
minGain = -45;
maxGain = 45;
aspRatio = 0.4;
ResourceFunction["PlotGrid"][{
  {Show[{BodePlot[tfModelRes[2 Pi s] /. unloadedLR /. param, {minFreq, maxFreq},
      GridLines → Automatic, ImageSize → 200, AspectRatio → aspRatio,
      BaseStyle → {"Times", 12}, PlotLayout → "Magnitude", PlotStyle → Blue,
      PlotLegends → {"Unloaded"}, PlotRange → {{minMult, maxMult}, {minGain, maxGain}}],
     BodePlot[tfModelRes[2 Pi s] /. alumLR /. param, {minFreq, maxFreq},
      PlotLayout → "Magnitude", PlotStyle → Gray, PlotLegends → {"Aluminum"}],
     BodePlot[tfModelRes[2 Pi s] /. ssLR /. param, {minFreq, maxFreq}, PlotLayout →
       "Magnitude", PlotStyle → {Dashed, Magenta}, PlotLegends → {"Stainless Steel"}],
     BodePlot[tfModelRes[2 Pi s] /. steelLR /. param, {minFreq, maxFreq},
      PlotLayout → "Magnitude", PlotStyle → Orange, PlotLegends → {"Steel"}]
    }, Frame → True, FrameLabel → {None, "Gain (dB)"}, FrameStyle → Black]}, {
   Show[{BodePlot[tfModelRes[2 Pi s] /. unloadedLR /. param,
      {minFreq, maxFreq}, GridLines → Automatic, ImageSize → 200,
      AspectRatio → aspRatio, BaseStyle → {"Times", 12}, PlotLayout → "Phase",
      PlotStyle → Blue, PlotRange → {{minMult, maxMult}, {minDeg, maxDeg}},
      FrameTicks → {{{-90, -45, 0, 45, 90}, None}, {Automatic, None}},
      GridLines → {Automatic, {-90, -45, 0, 45, 90}}],
     BodePlot[tfModelRes[2 Pi s] /. alumLR /. param, {minFreq, maxFreq}, PlotLayout →
       "Phase", PlotStyle → Gray, PlotRange → {{minMult, maxMult}, {minDeg, maxDeg}}],
     BodePlot[tfModelRes[2 Pi s] /. ssLR /. param, {minFreq, maxFreq}, PlotLayout → "Phase",
      PlotStyle → {Dashed, Magenta}, PlotRange → {{minMult, maxMult}, {minDeg, maxDeg}}],
     BodePlot[tfModelRes[2 Pi s] /. steelLR /. param, {minFreq, maxFreq}, PlotLayout →
       "Phase", PlotStyle → Orange, PlotRange → {{minMult, maxMult}, {minDeg, maxDeg}}]
    }, Frame → True, FrameLabel → {None, "Phase (°)"}, FrameStyle → Black]}
 }, FrameLabel → {"Frequency (Hz)", None}, BaseStyle → {"Times", 12}]
```

Out[57]=

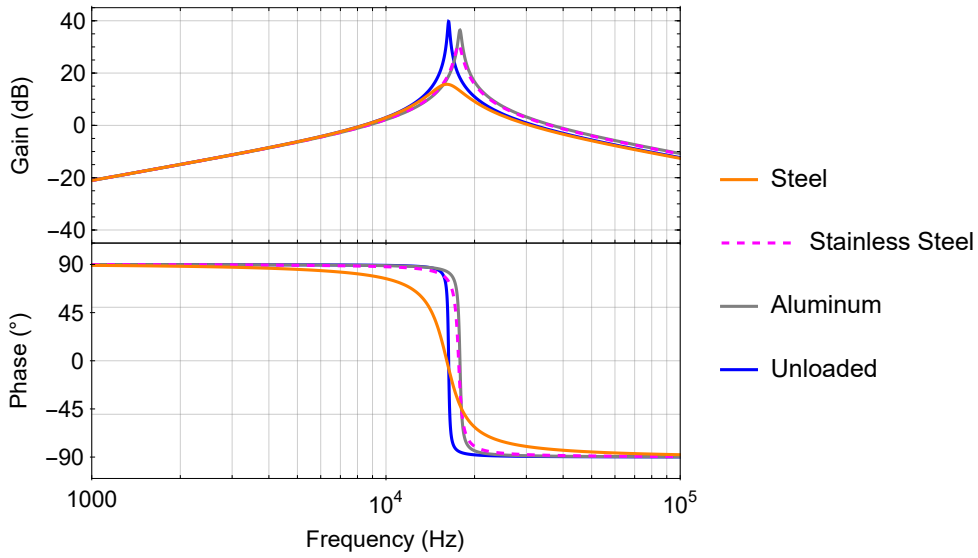

Describing function

In[58]:=
```
descFunctParam = <|c → busVolt / 43 /. param|>; (*c=outputHeight, a=inputHeight*)
na = 4 c / (π a);
k = 1 / na /. descFunctParam;
Row[{"N[a] = ", na, " = ", na /. descFunctParam // TraditionalForm}]
```

Out[61]=

$$N[a] = \frac{4\,c}{a\,\pi} = \frac{480\,\sqrt{2}}{43\,\pi\,a}$$

Nyquist plot analysis

In[62]:=
```
Show[{
  ParametricPlot[{Re[k], Im[k]}, {a, 0, 3000}, AspectRatio → 1,
   PlotRange → {{0, 550}, {-300, 300}}, PlotStyle → Red, Frame → True,
   GridLines → Automatic, PlotLegends → {"1/N(A)"}, FrameLabel → {"Re", "Im"},
   ImageSize → 200, BaseStyle → {"Times", 12}, FrameStyle → Black],
  NyquistPlot[SystemsModelSeriesConnect[TransferFunctionModel[
     na /. a → 1 /. descFunctParam, s], tfModelRes /. unloadedLR /. param],
   PlotLegends → {"G(ȷω) Unloaded"}, PlotPoints → 500, PlotStyle → Blue],
  NyquistPlot[SystemsModelSeriesConnect[
    TransferFunctionModel[na /. a → 1 /. descFunctParam, s], tfModelRes /. alumLR /. param],
   PlotLegends → {"G(ȷω) Aluminum"}, PlotPoints → 500, PlotStyle → Gray],
  NyquistPlot[SystemsModelSeriesConnect[
    TransferFunctionModel[na /. a → 1 /. descFunctParam, s], tfModelRes /. steelLR /. param],
   PlotLegends → {"G(ȷω) Steel"}, PlotPoints → 500, PlotStyle → Orange],
  NyquistPlot[SystemsModelSeriesConnect[
    TransferFunctionModel[na /. a → 1 /. descFunctParam, s], tfModelRes /. ssLR /. param],
   PlotLegends → {"G(ȷω) Stainless Steel"}, PlotPoints → 500, PlotStyle → Magenta]
 }]
```

Out[62]=

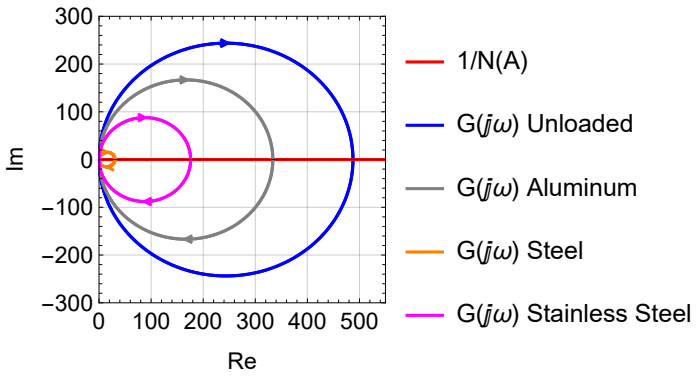

In[63]:=
```
Chop[NSolve[k == {tfModeljw /. unloadedLR /. param} &&
    Im[tfModeljw /. unloadedLR /. param] == 0 && Im[ω] == 0]]
Chop[NSolve[
  k == {tfModeljw /. alumLR /. param} && Im[tfModeljw /. alumLR /. param] == 0 && Im[ω] == 0]]
Chop[NSolve[k == {tfModeljw /. steelLR /. param} &&
    Im[tfModeljw /. steelLR /. param] == 0 && Im[ω] == 0]]
Chop[
 NSolve[k == {tfModeljw /. ssLR /. param} && Im[tfModeljw /. ssLR /. param] == 0 && Im[ω] == 0]]
```

NSolve: NSolve was unable to solve the system with inexact coefficients. The answer was obtained by solving a corresponding exact system and numericizing the result.

Out[63]=
$$\{\{a \to 0, \omega \to 0\}, \{a \to 487.525, \omega \to 102\,596.\}, \{a \to 487.525, \omega \to -102\,596.\}\}$$

NSolve: NSolve was unable to solve the system with inexact coefficients. The answer was obtained by solving a corresponding exact system and numericizing the result.

Out[64]=
$$\{\{a \to 0, \omega \to 0\}, \{a \to 333.662, \omega \to -112\,087.\}, \{a \to 333.662, \omega \to 112\,087.\}\}$$

NSolve: NSolve was unable to solve the system with inexact coefficients. The answer was obtained by solving a corresponding exact system and numericizing the result.

Out[65]=
$$\{\{a \to 0, \omega \to 0\}, \{a \to 30.6626, \omega \to -101\,132.\}, \{a \to 30.6626, \omega \to 101\,132.\}\}$$

NSolve: NSolve was unable to solve the system with inexact coefficients. The answer was obtained by solving a corresponding exact system and numericizing the result.

Out[66]=
$$\{\{a \to 0, \omega \to 0\}, \{a \to 175.861, \omega \to -110\,905.\}, \{a \to 175.861, \omega \to 110\,905.\}\}$$

Limit cycle simulation

Relay Non-linearity Simulation - Changing LR

State equation/parameters

In[72]:=
```
tf = 0.02;
swTime = 0.01;
states = {x1[t], x2[t], x3[t], h[t], l[t], r[t], e[t], e'[t], tn[t], f[t]};
(*x1[t]=Mutual Inductance Current,
x2[t]=Workcoil Inductance Current, x3[t]=Capacitor Voltage*)
hamiltonian = 1 / 2 l x2[t]^2 + 1 / 2 capC x3[t]^2;
eq1 = 1 / lm u[t];
eq2 = 1 / l[t] (u[t] - x2[t] r[t] - x3[t]);
eq3 = 1 / capC (x2[t]);
ode = {
    x1'[t] == eq1,
    x2'[t] == eq2,
    x3'[t] == eq3,
    l'[t] == 0,
    r'[t] == 0,
    h'[t] == D[hamiltonian, t] /. l → l[t],
    e'[t] == x2[t]^2 r[t]
   };
ic = {x1[0] == 0, x2[0] == 0, x3[0] == 0, h[0] == 0,
    l[0] == ls /. unloadedLR, r[0] == rs /. unloadedLR, e[0] == 0, tn[0] == 0, f[0] == 0};
input = <|u[t] → c Sign[x2[t]] /. descFunctParam|>;
Plot[u[t] /. input, {x2[t], -2, 2}, ImageSize → 250, Frame → True,
 FrameLabel → {"Input", "Output"}, BaseStyle → {"Times", 12}]
```

Out[82]=

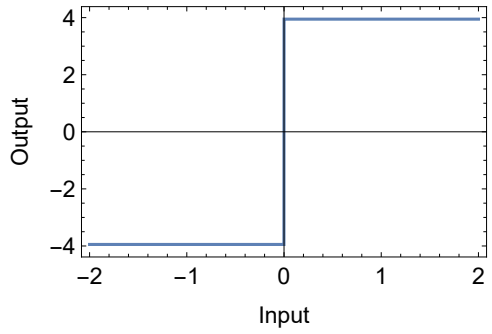

Simulation

In[83]:=
```
sys = Flatten[{ode /. input /. param, ic,
    WhenEvent[t > swTime, l[t] → ls] /. alumLR,
    WhenEvent[t > swTime, r[t] → rs] /. alumLR,
    WhenEvent[x2[t] == 0, {f[t] → 0.5 / (t - tn[t]), tn[t] → t}]
   }];
% // MatrixForm
```

Out[84]//MatrixForm=

$$\begin{pmatrix}
x_1'[t] == 214\,565.\,\text{Sign}[x_2[t]] \\
x_2'[t] == \frac{\frac{120}{43}\sqrt{2}\,\text{Sign}[x_2[t]] - r[t]\,x_2[t] - x_3[t]}{l[t]} \\
x_3'[t] == 71\,225.1\,x_2[t] \\
l'[t] == 0 \\
r'[t] == 0 \\
h'[t] == l[t]\,x_2[t]\,x_2'[t] + 0.00001404\,x_3[t]\,x_3'[t] \\
e'[t] == r[t]\,x_2[t]^2 \\
x_1[0] == 0 \\
x_2[0] == 0 \\
x_3[0] == 0 \\
h[0] == 0 \\
l[0] == 6.76668 \times 10^{-6} \\
r[0] == 0.0103072 \\
e[0] == 0 \\
tn[0] == 0 \\
f[0] == 0 \\
\text{WhenEvent}\left[t > \text{swTime}, l[t] \to 5.66925 \times 10^{-6}\right] \\
\text{WhenEvent}[t > \text{swTime}, r[t] \to 0.0150602] \\
\text{WhenEvent}\left[x_2[t] == 0, \left\{f[t] \to \frac{0.5}{t - tn[t]}, tn[t] \to t\right\}\right]
\end{pmatrix}$$

In[85]:=
```
sim = NDSolve[sys, states, {t, 0, tf}, DiscreteVariables → {tn, f}];
```

In[86]:=
```
NMaximize[{x2[t] /. sim // First, 0 ≤ t ≤ 0.01}, t]
NMaximize[{x2[t] /. sim // First, 0.015 ≤ t ≤ tf}, t]
```

Out[86]=
```
{487.288, {t → 0.009998}}
```

Out[87]=
```
{333.675, {t → 0.0173979}}
```

In[88]:=
```
NMaximize[{x3[t] /. sim // First, 0 ≤ t ≤ 0.01}, t]
NMaximize[{x3[t] /. sim // First, 0.015 ≤ t ≤ tf}, t]
```

Out[88]=
```
{338.042, {t → 0.0087885}}
```

Out[89]=
```
{212.034, {t → 0.0198787}}
```

In[90]:=
```
NMaximize[{e'[t] /. sim // First, 0 ≤ t ≤ 0.01}, t]
NMaximize[{e'[t] /. sim // First, 0.015 ≤ t ≤ tf}, t]
```

Out[90]=
```
{2447.44, {t → 0.009998}}
```

Out[91]=
```
{1676.78, {t → 0.017482}}
```

In[92]:=
```
t1init = 0.005;
t2init = 0.01;
t1final = 0.015;
t2final = 0.02;
1 / (t2init - t1init) Integrate[e'[t] /. sim, {t, t1init, t2init}] /. sim
1 / (t2final - t1final) Integrate[e'[t] /. sim, {t, t1final, t2final}] /. sim
```

Out[96]=
```
{{1212.61}}
```

Out[97]=
```
{{837.58}}
```

Plots

In[98]:=
```
tiPlot = 0.0098;
tfPlot = 0.0102;
tStartup = 0.0004;
ResourceFunction["CombinePlots"][
 MyPlot[x2[t] /. sim, 0, tStartup, "Time (s)", "Amp", Automatic, Automatic, 40, {"x2[t]"}],
 MyPlot[u[t] /. input /. sim, 0, tStartup, "Time (s)", "Volt",
  ColorData[97][2], Automatic, 40, {"u[t]"}], "AxesSides" → "TwoY",
 FrameStyle → {{ColorData[97][1], ColorData[97][2]}, Automatic}]
ResourceFunction["CombinePlots"][MyPlot[x2[t] /. sim, tiPlot,
  tfPlot, "Time (s)", "Amp", Automatic, Automatic, 40, {"x2[t]"}],
 MyPlot[u[t] /. input /. sim, tiPlot, tfPlot, "Time (s)", "Volt",
  ColorData[97][2], Automatic, 40, {"u[t]"}], "AxesSides" → "TwoY",
 FrameStyle → {{ColorData[97][1], ColorData[97][2]}, Automatic}]
```

Out[101]=

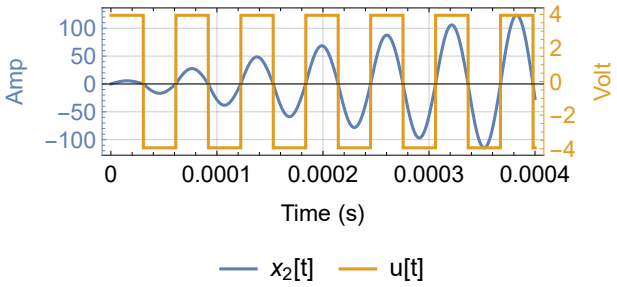

Out[102]=

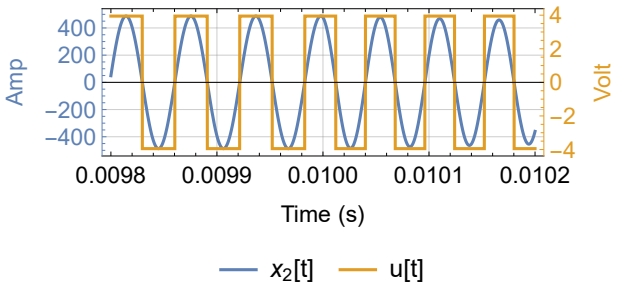

In[103]:=

```
ResourceFunction["CombinePlots"][MyPlot[x2[t] /. sim, tiPlot, tfPlot, "Time (s)",
  "Amp", Automatic, Automatic, 40, {"x2[t]"}], MyPlot[x3[t] /. sim, tiPlot,
  tfPlot, "Time (s)", "Volt", ColorData[97][2], Automatic, 40, {"x3[t]"}],
 "AxesSides" → "TwoY", FrameStyle → {{ColorData[97][1], ColorData[97][2]}, Automatic}]
```

Out[103]=

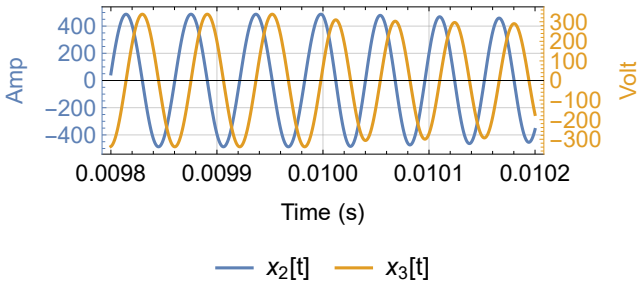

In[104]:=

```
tfPlot = tf;
MyPlot[x2[t] /. sim, 0, tfPlot, "Time (s)", "Volt", Automatic, 300, 40, {"x2[t]"}]
MyPlot[x3[t] /. sim, 0, tfPlot, "Time (s)", "Amp", Automatic, 300, 40, {"x3[t]"}]
```

Out[105]=

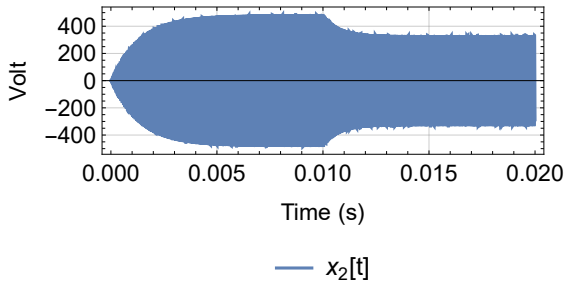

Out[106]=

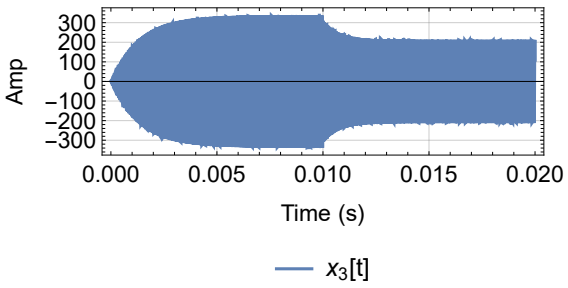

In[107]:=

```
MyPlot[10^6 l[t] /. sim, 0, tfPlot, "Time (s)", "μH", Automatic, Automatic, 40, ""]
MyPlot[10^3 r[t] /. sim, 0, tfPlot, "Time (s)", "mΩ", Automatic, Automatic, 40, ""]
```

Out[107]=

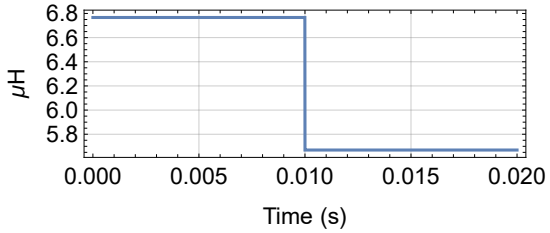

Out[108]=

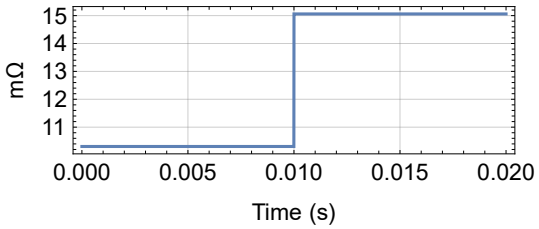

In[109]:=
```
MyPlot[1000 h[t] /. sim, 0, tfPlot, "Time (s)",
 "mJ", Automatic, Automatic, 40, {"Hamiltonian"}]
MyPlot[e[t] /. sim, 0, tfPlot, "Time (s)", "Joules", Automatic, Automatic, 40, {"Energy"}]
MyPlot[e'[t] / 1000 /. sim, 0, tfPlot, "Time (s)", "kW", Automatic, 300, 40, {"Power"}]
```

Out[109]=

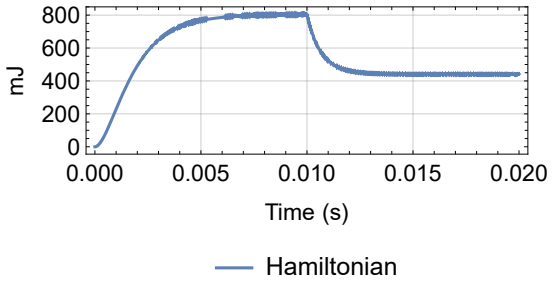

Out[110]=

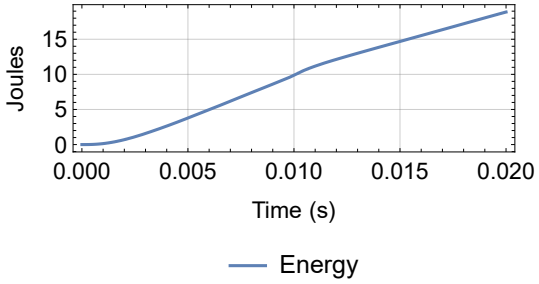

Out[111]=

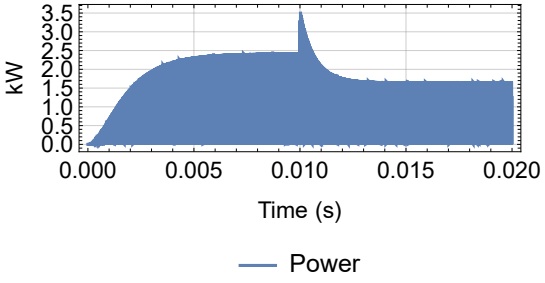

In[112]:=
```
MyPlot[x₁[t] /. sim, 0, tfPlot, "Time (s)", "Amp", Automatic, 300, 40, "x₁[t]"]
```

Out[112]=

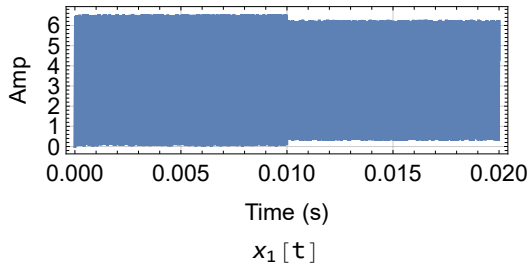

In[113]:=
```
fResInital = 1 / (2 Pi Sqrt[ls capC]) /. unloadedLR /. param;
fResFinal = 1 / (2 Pi Sqrt[ls capC]) /. alumLR /. param;
```

In[115]:=
```
Show[{
  MyPlot[f[t] /. sim, 0.0002, tfPlot,
   "Time (s)", "Hz", Automatic, Automatic, 40, {"Sim Freq"}],
  ListLinePlot[
   {{0, fResInital}, {swTime, fResInital}, {swTime, fResFinal}, {tf, fResFinal}},
   PlotStyle → {Red, Dashed}, PlotLegends → Placed[{"Calc Freq"}, Below]]
 }, PlotRange → {{0, tf}, {16000, 18000}}]
MyPlot[tn[t] /. sim, 0, tfPlot, "Time (s)", "tn (s)", Automatic, Automatic, 40, {"Time"}]
```

Out[115]=

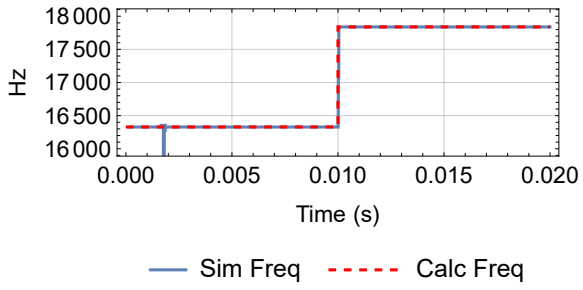

Out[116]=

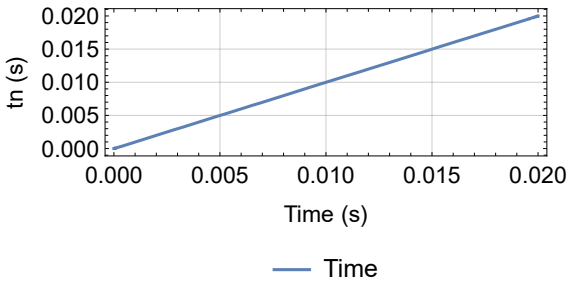

Frequency Calculation

In[117]:=
```
2 Pi f[t] /. sim /. t → 0.005
initalFSim = f[t] /. sim /. t → 0.005 // First
```

Out[117]=
```
{102 593.}
```

Out[118]=
```
16 328.1
```

In[119]:=
```
2 Pi f[t] /. sim /. t → 0.015
finalFSim = f[t] /. sim /. t → 0.015 // First
```

Out[119]=
```
{112 079.}
```

Out[120]=
```
17 837.9
```

In[121]:=
```
initalFDiff = PDiff[fResInital, initalFSim]
finalFDiff = PDiff[fResFinal, finalFSim]
```

Out[121]=
```
0.00275618
```

Out[122]=
```
0.0070225
```

In[123]:=
```
Export["NyquistSimulation.pdf", EvaluationNotebook[]];
```

Appendix B

Hardware Schematic

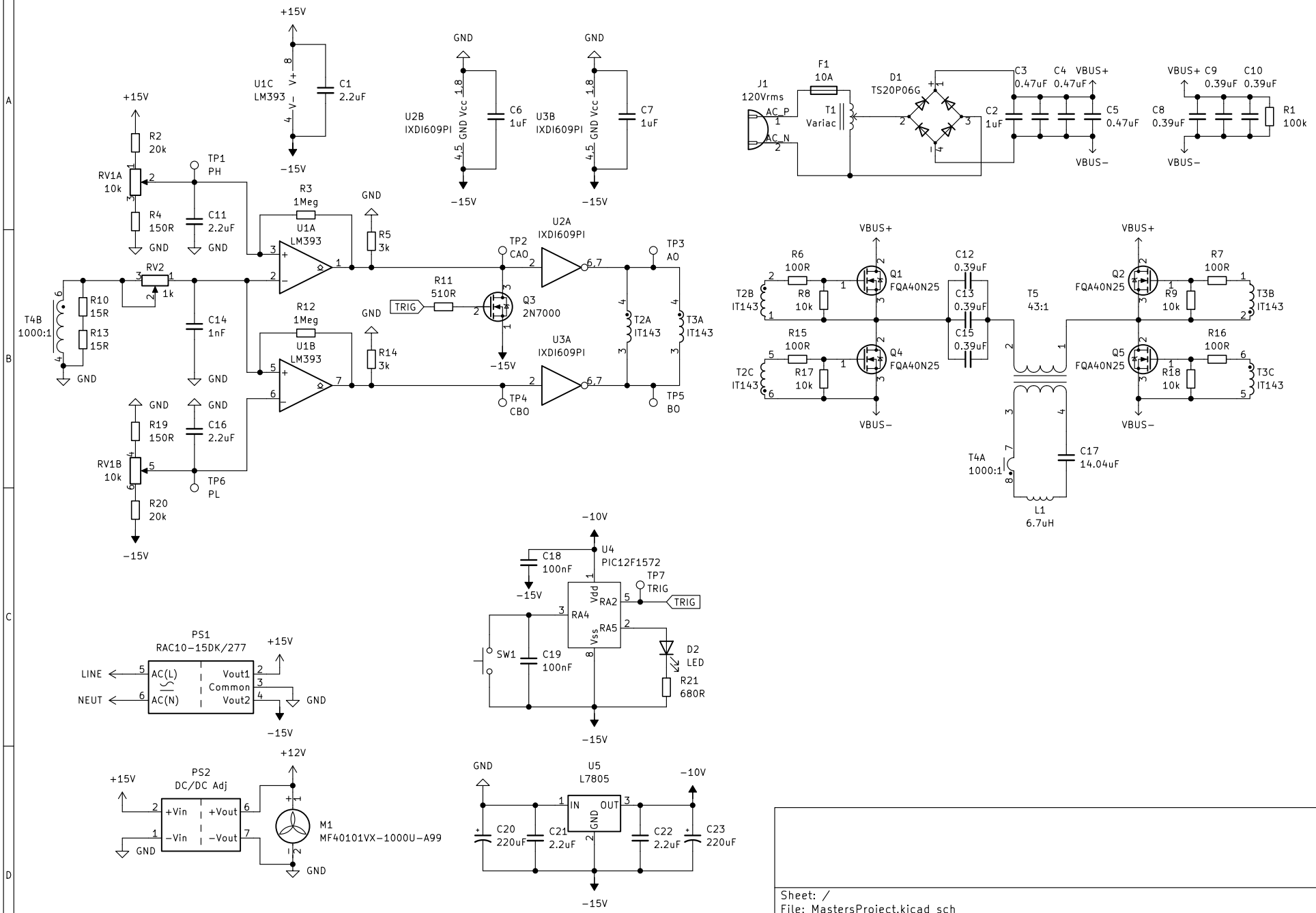

Sheet: /	
File: MastersProject.kicad_sch	
Title: Self−Oscillating Induction Heater	
Size: USLetter	Date: 2022−11−26
KiCad E.D.A. eeschema (6.0.6)	Id: 1/1

Rev: B

Appendix C

Pulse Generator Code

MPLAB X IDE was used for development. The Pickit 3 was used for programming.

```
1  /*
2   * File:  CONFIG.h
3   * Author: Patrick Rice
4   *
5   */
6
7  #ifndef XC_HEADER_TEMPLATE_H
8  #define XC_HEADER_TEMPLATE_H
9
10 // PIC12F1572 Configuration Bit Settings
11
12 // CONFIG1
13 #pragma config FOSC = INTOSC    // (INTOSC oscillator; I/O function on↩
       CLKIN pin)
14 #pragma config WDTE = OFF       // Watchdog Timer Enable (WDT disabled↩
     )
15 #pragma config PWRTE = ON       // Power-up Timer Enable (PWRT enabled↩
     )
16 #pragma config MCLRE = ON       // MCLR Pin Function Select (MCLR/VPP ↩
     pin function is MCLR)
17 #pragma config CP = OFF         // Flash Program Memory Code ↩
     Protection (Program memory code protection is disabled)
18 #pragma config BOREN = ON       // Brown-out Reset Enable (Brown-out ↩
     Reset enabled)
19 #pragma config CLKOUTEN = OFF   // Clock Out Enable (CLKOUT function ↩
     is disabled. I/O or oscillator function on the CLKOUT pin)
20
21 // CONFIG2
22 #pragma config WRT = OFF        // Flash Memory Self-Write Protection ↩
     (Write protection off)
```

```
23 #pragma config PLLEN = OFF       // PLL Enable (4x PLL enabled)
24 #pragma config STVREN = ON       // Stack Overflow/Underflow Reset ↩
       Enable (Stack Overflow or Underflow will cause a Reset)
25 #pragma config BORV = LO         // Brown-out Reset Voltage Selection (↩
       Brown-out Reset Voltage (Vbor), low trip point selected.)
26 #pragma config LPBOREN = OFF     // Low Power Brown-out Reset enable ↩
       bit (LPBOR is disabled)
27 #pragma config LVP = OFF         // Low-Voltage Programming Enable (Low↩
       -voltage programming enabled)
28
29 #include <xc.h>
30
31 #endif /* XC_HEADER_TEMPLATE_H */
```

```c
/*
 * File:   main.c
 * Author: Patrick Rice
 *
 * Created on August 2, 2022, 9:39 PM
 */
#include "CONFIG.h"

#define _XTAL_FREQ 16000000

void __interrupt() isr()
{
    LATA5=1;
    LATA2=1;
    __delay_us(15.3); //TRIG low time
    LATA2=0;
    __delay_ms(2000); //Switch de-bouncing
    LATA5=0;
    IOCAF=0;
}

void main(void) {
    //Osc
    OSCCONbits.IRCF=0b1111; //16MHz

    //WPU
    OPTION_REGbits.nWPUEN=0;
    WPUA4=1; //WPU on button input

    //Ports
    ANSELA=0x00;
    TRISA4=1; //button input
    TRISA2=0; //TRIG output
    TRISA5=0; //Busy LED output

    //Interrupt
    INTCONbits.GIE=1;
    INTCONbits.IOCIE=1;
    IOCAN4=1; //Interrupt when button is pressed (negative-edge)

    LATA2=0;
}
```